Reconstructing the P–T–t evolution recorded in garnet through growth and multicomponent diffusion modelling

Ben S. Knight

School of Earth and Planetary Sciences, Curtin University, Australia

ben.knight@curtin.edu.au

Chris Clark

School of Earth and Planetary Sciences, Curtin University, Australia

Ian C.W. Fitzsimons

School of Earth and Planetary Sciences, Curtin University, Australia

running title: Multicomponent diffusion in garnet

keywords: garnet, diffusion, Norway, Western Gneiss Region, high-pressure

Abstract

Interpreting the P–T evolution of a region recorded in garnet requires understanding of how the major elements in garnet (Fe, Mg, Mn and Ca) are modified by diffusion. We present an integrated approach that combines thermodynamic modelling with `MAGEMin` and multicomponent diffusion modelling using `UWDiffusion`, built on `underworld3`, to constrain the P–T–t evolution of a garnet pyroxenite from the Western Gneiss Region, Norway. We use the differential evolution minimisation technique to first estimate prograde P–T conditions from intersecting garnet end-member isopleths, which indicate garnet growth occurred between 9.5 and 14 kbar at isothermal conditions (∼475 °C) and then records burial and heating up to 19 kbar and 580°C. Peak conditions of above 20 kbar and ∼650°C were attained based on the lack of amphibole present in the sample and amphibole stability from thermodynamic modelling. Although thermodynamic modelling predicts garnet stability up to peak conditions, local depletion of garnet-forming elements stops growth. The modelling reveals that the preservation of compositional zoning indicates that temperatures remained below ∼700°C during exhumation, preventing substantial diffusional re-equilibration. Thermodynamic modelling reveals that the measured bulk stabilises epidote rather than the observed zoisite and a systematic investigation of the epidote–zoisite transition as a function of Fe_2O_3 content demonstrates that zoisite is stable only when the effective matrix Fe_2O_3 drops below ∼1.0 wt%, highlighting a prograde redox transition as the rock subducted, which coincides with garnet growth ceasing. This integrated approach demonstrates how coupling thermodynamic and diffusion modelling can be utilised to resolve the P–T–t record of a region through the observed mineral assemblage and garnet zoning.

1 Introduction

Garnet is one of the most important mineral in metamorphic petrology (Baxter et al., 2017). Its importance is due to the fact that compositional changes in its major cations can be directly linked to the variation in pressure and temperature (P–T) conditions during metamorphism (Faryad and Ježek, 2019; Florence and Spear, 1991; Tinkham and Ghent, 2005; Tracy et al., 1976; Caddick et al., 2010; Spear and Selverstone, 1983; Spear et al., 1984). The conditions are recorded in the compositional zoning of the four garnet end-members almandine (Fe), pyrope (Mg), spessartine (Mn) and grossular (Ca) (Tracy et al., 1976; Spear and Selverstone, 1983; Spear et al., 1984; Perchuk and Philippot, 1997) with the proportions of each determined by the pressure, temperature and effective bulk rock composition at the time of formation (Evans, 2004; Spear et al., 2014; Spear and Wolfe, 2018; Lanari and Engi, 2017; Konrad-Schmolke et al., 2005). However, the compositional changes (i.e. compositional zoning) in end-member proportions recorded in the garnet from core to rim can be modified by diffusion at temperatures above ∼700 °C for a ∼500 μm in diameter garnet (Caddick et al., 2010; Smit et al., 2013; Faryad et al., 2022; Gaidies et al., 2022).

Diffusion of the major cations in garnet is coupled (Anderson and Buckley, 1973; Loomis and Nimick, 1982; Loomis et al., 1985; Elphick et al., 1985; Chakraborty and Ganguly, 1991, 1992), where the movement of each cation is not independent but influenced by the concentration and diffusivity of the others. This phenomenon, known as multicomponent diffusion, is the simultaneous and interdependent migration of multiple chemical species within a crystal lattice (Lasaga, 1979; Borinski et al., 2012), making the system more complex than unary and binary species diffusion.

In garnet, multicomponent diffusion is particularly complex due to the four component system, with the interaction of Fe, Mg, Mn and Ca cations that diffuse at different rates under varying metamorphic conditions (Tracy et al., 1976; Spear et al., 1984; Spear, 1989; Chakraborty and Ganguly, 1992, 1991). During high-temperature events, diffusion can completely erase zoning patterns, removing the record of earlier metamorphic stages and can

imprint retrograde conditions instead (Pattison and Bégin, 1994; Weyer et al., 1999; Fernando et al., 2003). At lower temperatures, where diffusion is limited, growth zoning is preserved and offers valuable insights into the prograde metamorphic history (Faryad and Ježek, 2019; Faryad et al., 2022; Gaidies et al., 2008; George and Gaidies, 2017; Gaidies et al., 2022; Caddick et al., 2010; Chakraborty and Ganguly, 1991; Borinski et al., 2012; Spear et al., 1984). Understanding the rates and mechanisms of multicomponent diffusion in garnet is therefore essential for interpreting zoning and reconstructing accurate pressure–temperature–time (P–T–t) paths.

Thermodynamic models can be used to understand the partitioning of chemical components between mineral phases over P–T space and identify the conditions at which garnet grows. The growth of garnet can be incorporated into numerical models that include multicomponent diffusion to understand how the P–T–t evolution alters the end-member fractions. These models incorporate experimentally determined diffusion coefficients and enable the simulation of compositional changes during garnet growth and exhumation. By modelling the coupled diffusion of Fe, Mg, Mn, and Ca, it becomes possible to quantify how thermal evolution, garnet size, and composition influence the redistribution of major cations along a pressure–temperature–time (P–T–t) path (Faryad and Ježek, 2019; Gaidies et al., 2022; George and Gaidies, 2017). This approach allows for the exploration of varying geological histories in which compositional zoning is established, preserved, partially modified or completely overprinted, offering insights into the thermal evolution of metamorphic terranes (Caddick et al., 2010; Chakraborty and Ganguly, 1991; Borinski et al., 2012).

In this study, we have developed a new numerical approach to model multicomponent diffusion that uses underworld3 and garnet growth modelling using MAGEMin. Underworld3 utilises SymPy that allows the multicomponent equation to be represented symbolically, where the diffusion coefficients for different cations and different minerals can be quickly substituted without changing code. Underworld3 also supports multimaterials, where adjacent phases can be modelled. We have developed a python package, phasetools, that

utilises MAGEMin for thermodynamic modelling, allowing the garnet growth and diffusion modelling to be performed in the same script. The development of these tools opens up the possibility to perform inter granular diffusion between grains while using MAGEMin to determine thermodynamic properties.

In this paper we focus on multicomponent diffusion within a single grain, presenting and validating the numerical implementation. We first benchmark the multicomponent diffusion implementation against previously published results to validate the numerical approach. We then apply the garnet growth and diffusion modelling to constrain the P–T–t evolution of a garnet pyroxenite from the Western Gneiss Region (WGR), Norway. This paper outlines two tools that can be used to investigate metamorphic histories recorded in garnet. (1) Estimating growth P–T conditions from intersecting isopleths using a minimisation technique between measured and modelled garnet end-member fractions and (2) garnet growth and multicomponent diffusion modelling to constrain the P–T–t path. Subsequent work will extend this framework to multimaterial domains (enabling intergranular diffusion and Fe–Mg exchange between garnet and adjacent minerals) and to three-dimensional grain geometries.

2 Methods

2.1 Thermodynamic modelling with MAGEMin

We utilise `MAGEMin` (Riel et al., 2022), a parallel C library accessible through Julia, to extract garnet abundances and corresponding chemistry along a P–T path for a given bulk rock composition. Gibbs free energy minimisations are performed in Julia and accessed via a python package called `PhaseTools` that uses the `JuliaCall` package (Rowley, 2022). This workflow takes advantage of `MAGEMin`'s parallel capabilities while allowing outputs to be processed in python and incorporated into `underworld3`. `MAGEMin` is used both to estimate pressure–temperature (P–T) conditions recorded in garnet end-members and to extract the garnet information used to model garnet growth along a pressure–temperature–time (P–T–t)

path.

2.1.1 Estimating P–T conditions from isopleths

We use `MAGEMin` to estimate the prograde P–T path for garnet growth by locating the isopleth intersections for almandine (Fe), pyrope, (Mg) spessartine (Mn) and grossular (Ca) values measured along an electron-probe microanalysis (EPMA) traverse. Similar approaches have previously been used for garnet (Moynihan and Pattison, 2013; Lanari et al., 2017) as well as for multi-phase minimisations (Mackay-Champion and Cawood, 2026). The differential evolution method (Qiang, 2014) is used to explore the P–T space and obtain estimates of pressure–temperature (P–T) conditions through intersecting isopleths, although other minimisation techniques can also be used. The differential evolution method searches for the global minimum of a multivariate objective function, i.e. it searches for the P–T point which produces the lowest difference between the observed and modelled proportions of the four garnet end-members (Fe, Mg, Mn, and Ca) at each point along the garnet profile, where we use the weighted root-mean square error:

$$f(P,T) = \sqrt{\frac{1}{N}\sum_{i=1}^{N}\left(\frac{X_i^{\text{model}}(P,T) - X_i^{\text{obs}}}{\sigma_i}\right)^2} \tag{1}$$

where σ_i is the uncertainty assigned to component i. We assigned an uncertainty of $\sigma_i = 0.02$ (mole fraction) to garnet end-member compositions measured by EPMA, a conservative value given that total uncertainty includes accuracy-related terms beyond the counting-statistics precision routinely achievable for major elements (Llovet, 2018; Ritchie and Newbury, 2012). This value accounts for measurement precision, accuracy-related systematic errors (e.g., matrix corrections), instrumental drift, and the weight percent-to-mole fraction conversion.

However, this approach is only valid if garnet growth occurred in, or close to, equilibrium with the bulk composition used for the modelling and zoning has not been sufficiently mod-

ified by later processes (Faryad et al., 2022; Caddick et al., 2010). Fractionation of garnet can also be included to best match observations to better constrain the P–T path, as the rim equilibrated with an effective bulk composition different from that of the entire rock sample. However, fractionation for determining P-T conditions is not explored here as we find the non-fractionating inversion provides good P–T estimates and find our growth model, that includes fractionation, is able to replicate the observed core-to-rim profiles based on these P–T estimates.

2.1.2 Garnet growth modelling

Using the P–T information gathered from intersecting isopleths, we then use `MAGEMin` to grow a population of garnets and select one for diffusion modelling. Several existing tools, such as Compositional Zoning Garnet Modelling (`CZGM`) (Faryad and Ježek, 2019) and `THERIA_G` (Gaidies et al., 2008), are capable of simulating garnet growth and diffusion along P–T–t paths. CZGM employs `PERPLE_X` (Connolly, 1990) for thermodynamic modelling and MATLAB for garnet growth calculations, while `THERIA_G` uses `Theriak` (de Capitani and Brown, 1987) to perform thermodynamic equilibrium calculations in Fortran and is run in the command line. `PhaseTools` with `MAGEMin` offers a streamlined, all-Python workflow that avoids switching between MATLAB, Fortran, and command-line tools. `PhaseTools` can be used to systematically map phase stability across various redox states and garnet growth modelling can be directly incorporated with multicomponent diffusion modelling in `UWDiffusion`, enabling various growth histories to be explored as well as multicomponent diffusion to be modelled within a single framework. The symbolic representation of the diffusion matrix also enables diffusion coefficient databases to be swapped without modifying the underlying code, facilitating systematic comparisons across published diffusion coefficients.

Our garnet growth model simulates a population of garnet crystals along a user-defined P–T–t path using equilibrium data from `MAGEMin`. The garnet growth model can simulate fractionation by incrementally removing newly formed garnet from the reactive bulk com-

position at each step, with the growth model approaching Raleigh fractionation if changes in P–T are infinitesimally small. This allows different scenarios to be tested, i.e. continuous vs discontinuous garnet growth (Konrad-Schmolke et al., 2005). If the path starts within the garnet stability field, either the initial volume can be set to zero to simulate a clean initial growth event or the initial volume can be used, allowing the model to incorporate an "instantaneous" core that reflects the overstepped volume at the start of the path (Spear and Wolfe, 2019; Nagurney et al., 2021; Spear et al., 2014; Waters and Lovegrove, 2002; Castro and Spear, 2017).

The garnet population is generated by applying a user-defined size distribution (e.g., normal or uniform) to the total thermodynamic volume, representing the final crystal size distribution once garnet has stopped growing. This creates distinct size classes, that nucleate at different times and finish growth at the same time to achieve the final distribution. Each garnet is modelled as a sphere with concentric zoning (Faryad et al., 2022; Gaidies et al., 2008), that grows as a series of shells of equal thickness. As these shells are added, they record the P–T conditions at that point along the P–T path through the chemical composition (Mg, Mn, Fe, and Ca). This process results in a population of garnets with realistic core-to-rim zoning profiles that reflect the garnets growth history, without alteration due to diffusion, with a single garnet used in the diffusion modelling.

2.2 Determining the diffusion flux

The Maxwell–Stefan (M–S) diffusion equation (Maxwell, 1867; Stefan, 1871) describes mass transport in multicomponent systems. For species i from a total of n species, the M–S equation is:

$$\nabla \xi_i = \sum_{\substack{j=1 \\ j \neq i}}^{n} \frac{\xi_i J_j - \xi_j J_i}{c_t D_{ij}^{\mathrm{MS}}}, \quad \text{for } i = 1, 2, \ldots, n, \tag{2}$$

where ξ_i is the mole fraction of species i, J_i is its diffusive flux, $c_t = \sum_i c_i$ is the total

concentration of the diffusing sublattice, and D_{ij}^{MS} is the Maxwell–Stefan pair diffusivity between species i and j. The pair diffusivities are taken to satisfy $D_{ij}^{\mathrm{MS}} = D_{ji}^{\mathrm{MS}}$.

For diffusion-only problems, the fluxes and mole fractions satisfy:

$$\sum_{i=1}^{n} J_i = 0, \tag{3a}$$

$$\sum_{i=1}^{n} \xi_i = 1. \tag{3b}$$

Eq. 3a defines the molar-average reference frame used in the diffusion formulation, while eq. 3b ensures that the mole fractions remain normalised during diffusion. Summing the M–S equations demonstrates that only $n-1$ equations are independent:

$$\sum_{i=1}^{n} \nabla \xi_i = -\sum_{i=1}^{n} \sum_{\substack{j=1 \\ j \neq i}}^{n} \frac{\xi_j J_i - \xi_i J_j}{c_t D_{ij}^{\mathrm{MS}}} = 0. \tag{4}$$

Using the final species as the dependent component, the independent equations can be written in matrix form as:

$$c_t \begin{pmatrix} \nabla \xi_1 \\ \nabla \xi_2 \\ \vdots \\ \nabla \xi_{n-1} \end{pmatrix} = -\mathbf{B} \begin{pmatrix} J_1 \\ J_2 \\ \vdots \\ J_{n-1} \end{pmatrix}, \tag{5}$$

where $\mathbf{B}$ is an $(n-1) \times (n-1)$ matrix with elements:

$$B_{ij} = \begin{cases} \xi_i \left(\dfrac{1}{D_{in}^{\mathrm{MS}}} - \dfrac{1}{D_{ij}^{\mathrm{MS}}} \right), & i \neq j, \\ \dfrac{1}{D_{in}^{\mathrm{MS}}} + \displaystyle\sum_{k \neq i}^{n-1} \xi_k \left(\dfrac{1}{D_{ik}^{\mathrm{MS}}} - \dfrac{1}{D_{in}^{\mathrm{MS}}} \right), & i = j. \end{cases} \tag{6}$$

Although the Maxwell–Stefan pair diffusivities are taken to be symmetric, the reduced matrix $\mathbf{B}$ is generally non-symmetric because its elements depend asymmetrically on the

mole fractions. Rearranging Eq. 5 gives

$$\begin{pmatrix} J_1 \\ J_2 \\ \vdots \\ J_{n-1} \end{pmatrix} = -c_t \mathbf{B}^{-1} \begin{pmatrix} \nabla \xi_1 \\ \nabla \xi_2 \\ \vdots \\ \nabla \xi_{n-1} \end{pmatrix}, \tag{7}$$

where:

$$\mathbf{B}^{-1} = \tilde{\boldsymbol{\mathcal{D}}}^{\mathrm{MS}} \tag{8}$$

is the reduced effective diffusion matrix. The flux of species i can therefore be expressed as:

$$\mathbf{J}_i = -c_t \sum_{j=1}^{n-1} \tilde{\mathcal{D}}_{ij}^{\mathrm{MS}} \nabla \xi_j, \quad 1 \leq i \leq n-1. \tag{9}$$

The model uses two coefficient pathways. Where Maxwell–Stefan pair diffusivities are available, the coefficients D_{ij}^{MS} are used to construct $\tilde{\boldsymbol{\mathcal{D}}}^{\mathrm{MS}}$. Where only independent tracer or self-diffusion coefficients are available, an effective diffusion matrix is calculated directly using the mean-field approximation for ideal ionic solutions (Lasaga, 1979):

$$\tilde{\mathcal{D}}_{ij}^{\mathrm{MF}} = D_i^* \delta_{ij} - \left(\frac{D_i^* \xi_i}{\sum_{k=1}^{N} D_k^* \xi_k} \right) \left(D_j^* - D_N^* \right). \tag{10}$$

Here, D_i^* is the independent tracer or self-diffusion coefficient for species i, and δ_{ij} is the Kronecker delta. Equation 10 generates an effective generalized-Fick diffusion matrix directly; it does not calculate the Maxwell–Stefan pair diffusivities D_{ij}^{MS}.

$$\delta_{ij} = \begin{cases} 1, & i = j, \\ 0, & i \neq j. \end{cases} \tag{11}$$

`UWDiffusion` (Knight and Clark, 2026), built on `underworld3` (Moresi et al., 2025), is

a finite-element code for modelling multicomponent diffusion of major cations in garnet. `underworld3` leverages `SymPy` (Meurer et al., 2017) to symbolically construct the diffusion matrix $\tilde{\mathcal{D}}$ and associated flux terms, with composition- and P–T-dependent diffusion coefficients substituted into the symbolic expressions at each time step. This enables composition-dependent cross-term diffusivities and model-agnostic swapping between diffusion coefficient databases without manual derivation or solver modification. Users may also define custom flux expressions, which `underworld3` solves directly. All meshes are constructed using Gmsh (Geuzaine and Remacle, 2009), supporting a range of geometries including the multi-layered garnet domains used here.

3 Benchmarking multicomponent diffusion

We first verify multicomponent diffusion has been implemented correctly in UWDiffusion. Multicomponent diffusion couples the flux of each component to gradients of all others, so small errors can result in incorrect solutions. Our benchmarking compares our implementation to previously published work. Only after matching the benchmarks do we apply the model to infer timescales and the P–T evolution from garnet zoning in the Western Gneiss Region.

3.1 Benchmark 1: Binary mixture

For the initial benchmark a simple two-component system is utilised (Chai et al., 2019; Crank, 1979):

$$\mathbf{J}_1 = -\mathbf{J}_2, \quad \xi_1 + \xi_2 = 1, \quad D_{12} = D_{21} = \mathcal{D} \tag{12}$$

Due to Eq. 9 the flux term J_i can be expressed as:

$$\mathbf{J}_i = -c_t \mathcal{D} \nabla \xi_i, \quad i = 1, 2 \tag{13}$$

which is the classic diffusion (Fick's) law with a constant diffusivity, and the concentration of ξ_2 is equal to 1 - ξ_1.

The benchmark initial concentration is as follows:

$$\xi_1(x) = \begin{cases} C_0 & \text{if } x < 0, \\ C_1 & \text{if } x \geq 0. \end{cases} \tag{14}$$

Where $C_0 = 0.9$, $C_1 = 0.1$ and $\mathcal{D} = 0.05$. The model is run in a domain from -6 to 6 in length (x) and -1 to 1 in height (y), with an element resolution of 96 x 96 and Neumann condition ($J_i = 0$) on all boundaries. This benchmark tests the planar diffusion implementation as there is no change in composition in the y direction.

The analytical solution for the concentration of xi_1 can be calculated by the following equation:

$$\xi_1 = \frac{C_0 + C_1}{2} + \frac{C_1 - C_0}{2} \operatorname{erf}\left(\frac{x}{2\sqrt{\mathcal{D}t}}\right), \tag{15}$$

The results in Fig. 1 show the numerical results obtained from `UWDiffusion` match the expected analytical solution from Eq. 15 for xi_1 at t=1 and t=5.

3.2 Benchmark 2: Ternary mixture

A three-component coupled diffusion model is also tested, which has previously been used to benchmark other numerical implementations of multi-component diffusion (Chai et al., 2019; Boudin et al., 2012; Geiser, 2015), and is an approximation to the experiment conducted by Duncan and Toor (1962).

The domain is a box, with a length (x) from 0 to 1 and height (y) from 0 to 1 which is discretised on a 50 x 50 quadrilateral grid and Neumann condition ($J_i = 0$) on all boundaries. This benchmark also tests the planar diffusion implementation as the concentration is constant in the y direction.

The initial concentrations in the x direction are as follows:

$$\xi_1(x) = \begin{cases} 0.8, & 0 \le x < 0.25, \\ 1.6(0.75 - x), & 0.25 \le x < 0.75, \\ 0, & 0.75 \le x \le 1. \end{cases} \tag{16a}$$

$$\xi_2 = 0.2, \quad 0 \le x \le 1, \tag{16b}$$

$$\xi_3 = 1 - \xi_1 - \xi_2. \tag{16c}$$

The benchmark uses prescribed Maxwell–Stefan pair diffusivities, with $D_{12}^{\mathrm{MS}} = D_{13}^{\mathrm{MS}} = 0.833$ and $D_{23}^{\mathrm{MS}} = 0.168$. These coefficients are substituted into the reduced Maxwell–Stefan formulation to obtain the effective matrix:

$$\tilde{\mathbf{D}}^{\mathrm{MS}} = \begin{bmatrix} D_{12}^{\mathrm{MS}} & 0 \\ \dfrac{D_{12}^{\mathrm{MS}} \xi_2 (D_{23}^{\mathrm{MS}} - D_{12}^{\mathrm{MS}})}{D_{23}^{\mathrm{MS}} \xi_1 - D_{12}^{\mathrm{MS}} \xi_1 + D_{12}^{\mathrm{MS}}} & \dfrac{D_{12}^{\mathrm{MS}} D_{23}^{\mathrm{MS}}}{D_{23}^{\mathrm{MS}} \xi_1 - D_{12}^{\mathrm{MS}} \xi_1 + D_{12}^{\mathrm{MS}}} \end{bmatrix}. \tag{17}$$

The resulting effective matrix is equivalent to the formulation outlined in Chai et al. (2019) and Geiser (2015).

The results in Fig. 2 show the `UWDiffusion` numerical solution matches the previously published numerical solutions outlined by Geiser (2015); Chai et al. (2019); Boudin et al. (2012). ξ_1 follows Fick's law due to $\mathrm{D}_{12} = \mathrm{D}_{13}$, where the cross-diffusion term is zero, which removes any dependency on the gradients of ξ_2 and ξ_3, with its flux is governed solely by its own concentration gradient. However, ξ_2 does show uphill diffusion over time which is not consistent with Fick's law, driven by the cross-diffusion term. The concentration of ξ_2 changes from an initial equilibrium state of 0.2 at $t = 0$ to a minimum value of 0.1581 at $t \approx 0.2$ before increasing again towards 0.2, similar to the results observed by Duncan and Toor (1962).

3.3 Benchmark 3: three-component garnet diffusion

This benchmark examines a ternary Fe–Mg–Ca diffusion system in garnet, with Ca as the dependent component and Mn neglected. It uses the published effective generalized-Fick diffusion matrix $\tilde{\mathbf{D}}$ from Vielzeuf and Saúl (2011), in which both Fe and Mg contain cross-diffusion terms. The effective matrix is prescribed directly; consequently, this benchmark tests the coupled flux implementation but does not test conversion from Maxwell–Stefan pair diffusivities or independent tracer coefficients.

Vielzeuf and Saúl (2011) used the initial concentrations (ξ_i) and $\tilde{D}$ matrix:

$$\xi_1 = Mg = \begin{cases} 0.461185, & x \leq 6\mu m, \\ 0.4569965, & else \end{cases}, \xi_2 = Fe = \begin{cases} 0.5190967, & x \leq 6\mu m, \\ 0.50997849, & else \end{cases}, \xi_3 = 1 - \xi_1 - \xi_2, \tag{18a}$$

$$\tilde{\mathbf{D}} = \begin{bmatrix} D_{MgMg} & D_{MgFe} \\ D_{FeMg} & D_{FeFe} \end{bmatrix} = \begin{bmatrix} 0.66\times10^{-19} & -4.74\times10^{-19} \\ -0.4\times10^{-19} & 4.5\times10^{-19} \end{bmatrix} \tag{18b}$$

The model presented by Vielzeuf and Saúl (2011) is planar diffusion (along a line in 1D) and is replicated in `UWDiffusion` by repeating initial concentrations in the y direction. The domain is 12 μm in length (x) and 1 μm in height (y) and has an element resolution of 300x25. No boundary conditions are prescribed, which results in Neumann boundaries ($J_i = 0$) on all sides. The model is run for a total of 518,400 seconds (6 days) to replicate the profiles of Vielzeuf and Saúl (2011).

The results in Fig. 3 show agreement between the `UWDiffusion` implementation and the diffusion profiles of Vielzeuf and Saúl (2011). The model reproduces the profiles for both Mg and Fe, including uphill diffusion of Mg. This behaviour results from the combined flux $\mathbf{J}_i = -c_t \sum_j \tilde{\mathcal{D}}_{ij} \nabla \xi_j$: the negative $\tilde{D}_{\mathrm{MgFe}}$ term is sufficiently large relative to $\tilde{D}_{\mathrm{MgMg}}$ to drive Mg against its own concentration gradient, whereas the smaller $\tilde{D}_{\mathrm{FeMg}}$ term means that Fe diffusion is more strongly controlled by its own concentration gradient.

3.4 Benchmark 4: Garnet diffusion along a P–T–t path

In this benchmark, we compare results from $CZGM$ (Faryad and Ježek, 2019) with our own implementation of multi-component diffusion. The $CZGM$ software contains an example to extract a garnet population from a pseudosection grid along a P–T–t path without the effects of fractionation. This benchmark is presented to test the garnet growth and diffusion implementation in `UWDiffusion`, not the growth model itself. In this benchmark garnet is diffusing after each growth step along the prograde path then transitions to diffusion only as there is no increase in volume along the retrograde path. During the garnet growth stage, the garnet grows outwards and has a total of 30 shells. As the garnet grows, the most recent growth shell has a fixed boundary condition. As the entire garnet is meshed initially, during the growth stage the outer shells also contain the same concentration as the most recent growth shell. Once garnet growth has finished, the concentration of the final shell is fixed for the remainder of the model.

We test diffusion in both a box and within an annulus, both in Cartesian coordinates, to compare results with diffusion in $CZGM$, which includes the functionality to represent diffusion in planar (along a line) or spherical (in a sphere) geometries as a one-dimensional line. Spherical coordinates are the best approximation for a concentric garnet with radial symmetry (composition varies only with distance from the core). Planar diffusion handles cases where spherical symmetry may not be a suitable approximation, e.g. from off-centre thin-section cuts, rim-only segments, or non-concentric zoning from resorption/embayment. The planar diffusion implementation in $CZGM$ is compared to a two-dimensional domain where the concentrations only vary horizontally, while the spherical diffusion model in $CZGM$ is compared with an annulus in 2D in `UWDiffusion`. The annulus represents cylindrical diffusion, that is between planar and spherical diffusion, and can be used to resolve non-radial effects while remaining computationally tractable but under-resolve diffusion due to neglecting the third dimension Ganguly and Tirone (1999) when compared to spherical models, highlighting a key limitation of diffusion models when utilising 2D approximations. For this

benchmark, independent diffusion coefficients are used for Fe, Mg and Mn. The Ca coefficient is approximated as $D^*_{\mathrm{Ca}} = D^*_{\mathrm{Mn}}/20$ (Faryad and Ježek, 2019). These coefficients are used as inputs to the mean-field approximation in Eq. 10 to calculate the composition-dependent effective diffusion matrix. The diffusion coefficients for each element are calculated as:

$$D = D_0 \cdot \exp\left(-\frac{Q}{RT}\right) \tag{19}$$

- D : Diffusion coefficient
- D_0 : Pre-exponential factor.
- Q : Activation energy for diffusion
- R : Universal gas constant (1.9872 cal K^{-1} mol^{-1})
- T : Absolute temperature (K)

using the values outlined in Table 1.

Table 1: Parameters for the independent Fe, Mg and Mn diffusion coefficients from Chakraborty and Ganguly (1992). The Ca coefficient is approximated as $D^*_{\mathrm{Ca}} = D^*_{\mathrm{Mn}}/20$ (Faryad and Ježek, 2019).

Element	D_0 [cm^2 s^{-1}]	Q [cal mol^{-1}]
Fe	6.36×10^{-4}	$65,824$ ($\pm 8,721$)
Mg	1.11×10^{-3}	$67,997$ ($\pm 8,973$)
Mn	5.15×10^{-4}	$60,569$ ($\pm 8,889$)

The results show that `UWDiffusion` is able to replicate the diffusion profiles from $CZGM$ when both are modelled in a planar geometry (4c). However, when comparing the spherical diffusion profiles from $CZGM$ with the 2D cylindrical annulus domain results from `UWDiffusion`, a discrepancy emerges, primarily in the Fe and Mn fractions, near the centre of the garnet. This arises because the 2D annulus represents a cylindrical geometry, where the geometric source term scales as $1/r$ rather than the $2/r$ of a sphere. The reduced flux convergence in the cylindrical case is most significant at small radii, and produces slower

effective diffusion at the garnet core, most noticeably for the fastest-diffusing elements (Fe and Mn).

These four benchmarks demonstrate that our implementation correctly handles: (1) Fickian diffusion in binary systems, (2) cross-term coupling in ternary systems, (3) uphill diffusion in quaternary garnet, and (4) produces results consistent with established garnet diffusion codes but neglects the effects of the third dimension that leads to underestimations in the amount of diffusion, primarily at the garnet core, therefore timescales and peak temperatures are inferred as minimums, as diffusion in spherical domains is faster Ganguly and Tirone (1999).

4 Estimating the P–T–t evolution of the southern Western Gneiss Region

The Western Gneiss Region (WGR) in Norway has a complex geological and metamorphic history. The region exhibits structural, petrographic, and thermobarometric zonation from southeast to northwest, reflecting varying burial and exhumation depths of both oceanic and continental crust during the collision between Baltica and Laurentia during the Scandian phase of the Caledonian Orogeny around 430 to 400 million years ago (Engvik et al., 2000; Labrousse et al., 2004; Hacker et al., 2010). The region has ¿30,000 km^2 of HP (¿12 kbar) and ¿5,000 km^2 of UHP (¿27 kbar) rocks exposed at the surface, with ∼2 vol% mafic rocks (Peterman et al., 2009).

In the northern part of the WGR, pressures reached up to 32 kbar and temperatures over 800°C as material was buried to depths of more than 120 km (Hacker et al., 2010), leading to the formation of eclogites (Cuthbert et al., 2000; Root et al., 2005; Hacker et al., 2010). The southern region has received less attention than the UHP regions of the central and northern domains but peak conditions have previously been estimated to be between 15 - 25 kbar and 590 - 720°C (Engvik et al., 2000; Martin and Duchêne, 2015). The pressure

and temperature decrease from north to south is thought to represent the subducting slab Labrousse et al. (2004). The exhumation of high-pressure rocks in the region is thought to have occurred rapidly, with units being exhumed by the Nordfjord-Sogn detachment zone within ≤10 Myr of peak metamorphism (Hacker et al., 2003, 2010).

We study a garnet-pyroxinite from Vardehia, with sample WGC18-016 from a mafic boudin enclosed within a foliated felsic gneiss, typical of those that dominate the bulk of the WGR, near Tyssedalsvatnet (61 18 49 N, 5 15 04 E) (Fig. 5a). The sample appears to be well-equilibrated at peak conditions, preserving the peak mineral assemblage of garnet, zoisite, quartz and clinopyroxene with accessory rutile. The sample has a well-developed foliation defined by oriented zoisite and clinopyroxene crystals that wrap sub-idioblastic garnet porphyroblasts (up to ∼5 mm) (Fig. 5b).

4.1 Insights from thermodynamic modelling of sample WGC18-016

We use `MAGEMin` with the 6.36 thermodynamic dataset (Holland and Powell, 2011) and metapelite extended (*mpe*) database to perform phase equilibria modelling for the WGC18-016 sample in the MnNCKFMASHTO (MnO–Na2O–CaO–K2O–FeO –MgO–Al2O3–SiO2–H2O–TiO2–O) system using the measured and reduced bulk chemical compositions listed in Table 2. The metapelite extended database, which is a combination of the metapelite (White et al., 2014) and metabasite (Green et al., 2016) databases, was used due to the inclusion of MnO and a clinopyroxene solution model, which is required to model garnets that contain all the cations (Fe, Mg, Mn and Ca) required for multicomponent diffusion modelling. We use all available pure and solution phase models when modelling sample WGC18-016. The method for determining the bulk rock chemistry is outlined in supplementary material S1 while the methods for determining the clinopyroxene and garnet chemistry are outlined in supplementary material S2. All FeO from the garnet EPMA is assumed to be Fe^{2+}. The peak mineral assemblage for sample WGC18-016 is characterised

by zoisite, garnet and clinopyroxene, with accessory quartz and rutile (Fig. 5).

We test both the metapelite extended and metabasite databases with the reduced bulk rock composition and find neither perfectly reproduces the observed mineral assemblage from the thin section. Both databases stabilise amphibole across all H_2O and Fe_2O_3 values tested at higher P–T conditions compared to zoisite (Fig. S1) and is consistent across tested datasets (6.2 and 6.36). This may be due to the complex amphibole a–x relations for metabasite compositions, uncertainties in the measured bulk composition, or open-system behaviour during metamorphism that is not captured by the equilibrium thermodynamic model. We do observe a decrease in the pressure and temperature of the amphibole-out location between datasets 6.2 and 6.36, which suggests the amphibole solution model may not be well calibrated close to eclogite facies conditions (Fig. S2). The stability of garnet, clinopyroxene and amphibole (Fig. 6) is fairly consistent across the measured and reduced bulk rock compositions tested (Table 2), with only zoisite stability varying between tested compositions. No zoisite is stable in the measured bulk rock composition, with epidote stable instead, and a lower bulk-O or higher-reduced model required to reproduce zoisite stability, which is consistent across databases (mpe and mb) and datasets (6.2, 6.36). A systematic investigation of the epidote–zoisite transition as a function of Fe_2O_3 content highlights that zoisite is stable only when the effective matrix Fe_2O_3 drops below ~1.0 wt% (Fig. S3). Under the tested reduced conditions (Fe_2O_3 = 0.5 wt%), zoisite becomes stable between 7 and 22.5 kbar at 550–650 °C (Fig. 6b).

The reduced bulk composition to stabilise zoisite results in diverging isopleths from the garnet core. The change in oxide state results in the grossular (Ca) and pyrope (Mg) isopleths diverging, resulting in no coherent intersection (Fig. 6b). The divergence of the core garnet isopleths under reduced conditions suggest the garnet formed in a oxidised environment represented by the measured bulk rock that subsequently transitioned to a more reduced state required to stabilise zoisite, although no constraints on the temporal evolution of the redox transition are available.

Oxide	SiO_2	Al_2O_3	CaO	MgO	FeO	K_2O	Na_2O	TiO_2	O	MnO	H_2O
Measured	44.76	8.88	12.31	16.43	8.33	0.05	1.36	0.03	0.87	0.11	6.86
Reduced	45.08	8.94	12.39	16.55	8.39	0.06	1.37	0.03	0.18	0.11	6.91

Table 2: Oxide list of measured and reduced bulk rock compositions used in thermodynamic modelling in mol%. The measured O values may represent the maximum oxidised state due to oxidisation of the sample at the surface. The method for determining the measured bulk rock composition is outlined in S1.

4.2 Determining the P–T prograde path from WGC18-016

The analysed garnet grain is one of the largest in the thin section and therefore most likely to have nucleated early and record the P–T evolution. The garnet in sample WGC18-016 exhibits distinct compositional zoning, with Mn-enriched and Mg-depleted cores transitioning to Mn-depleted and Mg-enriched rims (Fig. 7), with a detailed transverse taken across the grain at ∼50 micron step sizes Fig. 8) used to estimate the P–T path from intersecting isopleths. The zoning observed is characteristic of growth zoning during prograde metamorphism (Hollister, 1966; Loomis and Nimick, 1982). The garnet maps (Fig. 7) show Fe concentrations increasing slightly from the core toward the mantle before declining at the rim, while Ca displays only a minor decrease from core to rim. The preservation of these compositional profiles suggests limited modification due to diffusion and that primary growth zoning may have been retained. Although fractures are present, no alteration of end-members is observed in garnet adjacent to fractures, consistent with crack formation after diffusion ceased during exhumation.

We use the measured bulk rock composition to estimate the prograde P–T path using the technique outlined in section 2.1.1. The results (Fig. 8b) show that garnet growth initiated during a phase of near-isothermal burial at approximately 475 °C, with pressure increasing from 9.5 to 14 kbar (Fig. 8b), with the core plotting at an initial garnet volume of ∼1.5% (6a). Some P–T estimates plot between 14 and 20 kbar and 475 to 575 °C, but these estimates come from poorly constrained rims (Fig. 8b-8c). The P–T estimates at 20 kbar and 575 °C are close to the modelled peak zoisite stability from the reduced bulk

composition of 19 kbar 580 °C (Fig. 6b).

The misfit (Eq. 1) between the thermodynamic predictions and the measured EPMA data increases progressively toward the rim. These results show that while the original bulk rock composition (Table 2) provides a good representation of the rock composition for the initial nucleation P–T condition but becomes increasingly less representative of the reactive environment as growth continues. This is most likely due to two factors: (1) the fractionation of garnet-forming elements (Fe, Mg, Mn and Ca) from the bulk rock, altering the effective bulk rock composition, and (2) the bulk rock becoming more reduced during subduction, which is required to stabilise zoisite (Fig. 6). Additional constraints on temperature are provided by rutile grains from the sample. Zr-in-rutile thermometry records temperatures of 565 to 580 °C at 20 kbar using the Kohn (2020) thermometer (Fig. S4), providing minimum temperature estimates as no zircon is present in the rock.

4.3 Timing constraints on the P–T path

No geochronological constraints are available from this sample but constraints of burial and exhumation are extensively presented in the literature from the WGR. Garnet growth timing is constrained by Lu–Hf geochronology from the Vollstein eclogite yields an age of 410 ±3.1 Ma (Kylander-Clark et al., 2009) (sample K5622A) while whole-rock isochrons from the Vårdalsneset eclogite return ages of 409 ±12 (sample NOG12) and 403 ±13 Ma (sample NOG13) (Martin et al., 2010). Peak and retrograde timings are recorded from various geochronometers, with a U–Pb monazite age of 410 to 390 Ma (Holder et al., 2015; Hacker et al., 2015) recording the timing of peak temperature. U–Pb titanite preserves ages between 405 and 390 Ma (Holder et al., 2015; Hacker et al., 2015), while U–Pb rutile records ages of 400-375 Ma, recording the timing of retrograde cooling. Based on these geochronometers, we interpret the garnet Lu–Hf age to represent garnet growth initiation at 410 Ma as Lu strongly partitions into garnet as it nucleates (Anczkiewicz et al., 2007), peak conditions were reached at 400 Ma based on U–Pb monazite and titanite followed by 10 Myr of isothermal until 390

Ma. Finally the sample experienced a period of close to isobaric cooling to 580 °C at 385 Ma, based on the U–Pb rutile ages, following a typical subduction burial and exhumation path Duretz and Gerya (2013); Duretz et al. (2012)).

4.4 Garnet growth and diffusion modelling

Four parameters control the zoning recorded in the garnet, (1) the mineral reactions and resulting garnet growth and fractionation from the bulk rock, which determine the composition of each garnet growth stage from core to rim along the metamorphic P–T path; (2) the crystal size, with larger grains assumed to have commenced growth earlier and therefore preserve earlier stages of the P–T evolution; (3) the temperature over the entire path and peak temperature reached, with higher temperatures promoting diffusional modification of growth zonation, and (4) the duration of the entire path, with longer durations promoting diffusional modification (Caddick et al., 2010). While the timing of burial and exhumation is fairly well constrained from geochronometers, uncertainties remain regarding the P–T path of burial and exhumation of sample WGC18-016.

We use the approach described in Section 2.1 to predict garnet end-member fractions from `MAGEMin` from the measured bulk rock composition, with garnet fractionated at each P–T point. This information is then used to generate a normal distribution of 100 garnets along the prograde P–T path. The volumetric growth of each successive garnet shell is determined by the garnet volume assuming a spherical geometry, with each shell fractionated from the bulk rock as the garnet grows. During prograde garnet growth and diffusion, concentrations at the outer shell are fixed, assuming equilibrium between the bulk rock matrix and the external shell. Independent Fe, Mg and Mn diffusion coefficients are obtained from Table 1. The Ca coefficient is approximated as $D^*_{\mathrm{Ca}} = D^*_{\mathrm{Mn}}/20$. These coefficients are substituted into Eq. 19 and used in the mean-field approximation of Eq. 10 to calculate the composition-dependent effective diffusion matrix. We test three garnet crystal size distributions: (1) a narrow normal distribution ($\mu = 1800\ \mu m$, $\sigma = 50\ \mu m$) representing a population dominated

by early and large porphyroblast nucleation; (2) a normal distribution (μ = 1000 μm, σ= 200 μm) representing an intermediate population; and (3) a log-normal distribution (s = 0.5, median = 800 μm), consistent with the positively skewed crystal size distributions measured in metapelitic garnet (Gaidies et al., 2021; George and Gaidies, 2017). We find that the narrow normal distribution (1) best fits the observed EPMA data and use this crystal size distribution for all models (Fig. S6).

4.4.1 Testing *P–T–t* paths

We test two *P–T* paths to determine the peak conditions of WGC18-016. We assume once garnet growth has ceased it has depleted the local bulk composition of garnet-forming elements and zero flux of element fractions occurs across the outer shell after growth has finished and diffuses internally only. The first path peaks at peak zoisite composition, 19 kbar and 580 °C (Fig. 9a) while the second peaks at amphibole-out, 22 kbar and 650 °C (Fig. 9d). Both follow the isothermal path predicted from the isopleths at 475 °C between 9.5 and 14 kbar, then undergo increasing pressure and temperature to peak conditions. We model a 1800 μm garnet for the first path, to match the modelled garnet rim compositions with the analytical measurements, while we model a 2100 μm garnet for the second path to match the analytical measurements up to r = ~1800 μm.

We find that the growth profile from the first *P–T* path matches closely with the measured garnet isopleths from core to rim (Fig. 9b) and is not modified due to diffusion (Fig. 9c). The growth model from the second *P-T* path is also similar to the measured garnet isopleths up to 580 °C, however, the garnet volume increases rapidly between 580 °C and 650 °C (Fig. 9d), which results in much lower Fe (0.35) and higher Mg (0.4) compared to the measured values (0.54 and 0.21, respectively) at the rim (Fig. 9e), which are also unmodified by diffusion (Fig. 9f).

4.4.2 Testing overstepped growth

Isothermal paths have previously been interpreted as kinetic artifacts, or an "isothermal illusion" (Spear and Wolfe, 2018; Spear et al., 2014; Spear and Wolfe, 2019), arising from rapid, overstepped growth that outpaces thermal equilibration (Spear and Wolfe, 2019). In an overstepped scenario, the instantaneous growth of a finite garnet volume rapidly depletes the matrix in garnet-forming elements (particularly Mn), producing compositional profiles that replicate those of pressure-driven growth at constant temperature. We compare overstepped and continuous growth models to evaluate if the P–T-t path from garnet end-members (Fig. 8) could represent over-stepped growth.

The overstepped model incorporates an initial garnet volume that forms instantaneously at the overstepping point, accounting for the rapid removal of garnet-forming elements from the bulk rock. In this scenario, subsequent growth proceeds only once the equilibrium garnet volume exceeds the initial overstepped threshold. The thermodynamic modelling of the measured bulk rock expects an initial 1.5 vol% of garnet at estimated P–T point for the garnet core, which is used to model the overstepped growth. The second model assumes the initial garnet volume is set to zero at the start of the P–T path. Comparing these two end-members allows us to determine whether the apparent isothermal burial is a result of the prograde evolution or an "isothermal illusion" caused by overstepped nucleation (Spear and Wolfe, 2019). In both cases, the garnet is assumed to be isolated from the reactive bulk rock following the cessation of growth, with subsequent evolution governed by internal diffusion only.

Our model results show the overstepping model (Fig. 10b) produces a distinct compositional discontinuity in the garnet mantle. In contrast, the continuous growth model (Fig. 9b) results in a smooth compositional profile from the core through the mantle. Toward the rim, the profiles converge as late growth occurs under identical P–T conditions in both scenarios (Figs. 10a & 9a). The main difference between the overstepped (Fig. 10c) and continuous (Fig. 9c) growth model is the perseverance of these flat profiles at the core

in the overstepped model due to a lack of diffusion to equilibrate the garnet cores at the temperature-time paths tested. These results demonstrate that even if the cores are a result of overstepping, additional growth at the same temperature but higher pressure is required to match the garnet end-members observed in the EPMA profiles towards the mantle and the rim. The results show that garnet growth was primarily pressure-driven, supported by volume isopleths increasing near-perpendicular to pressure. This style of growth is characteristic of cold subduction environments, where tectonic burial is sufficiently rapid to prevent thermal equilibration as it buries (Simon et al., 2023; March et al., 2022), and aligns with P–T paths predicted by numerical models of slab subduction and eduction (Duretz and Gerya, 2013). The stability of garnet at trace volumes below ∼9.5 kbar at 475 °C in the metapelite extended database is due to the combination of the metapelite and metabasite databases, with the metabasite, which is more representative of the mafic protolith, showing garnet is unstable below ∼9.5 kbar at 475 °C (Fig. S5).

4.4.3 Constraints on peak temperature

We evaluate the peak T conditions of WGC18-016 based on the preservation of garnet compositional zoning. The close temporal overlap between U-Pb monazite ages (410–390 Ma; Holder et al. (2015); Hacker et al. (2015)) and U–Pb titanite ages (405–390 Ma) suggests peak temperatures were likely ≤700°C. Given that the U–Pb closure temperature (T_c) for titanite is typically between 550 and 650°C, higher peak temperatures would be expected to produce a larger discrepancy between monazite and titanite ages, while the lack of amphibole suggests temperatures above 650 °C (Fig. 6). To test the peak temperature and the sensitivity of garnet zoning to peak thermal conditions, we repeated the growth model along the entire path to amphibole-out at 22.5 kbar and vary the peak temperature up to 720°C. Our results show that peak temperature of 720°C lead to excessive smoothing of compositional zoning (Fig. 11). This is most pronounced in Fe and Mn profiles, which possess the highest diffusion coefficients in garnet at temperatures >550°C. Preservation of the measured core-to-rim

zoning therefore requires peak conditions ≤700°C. The use of a 2D annulus domain to model diffusion in garnet also underestimates the true extent of relaxation, as 3D (spherical) diffusion is faster, as outlined in section 3.4. Consequently, our 700°C limit represents a maximum estimate.

4.5 The evolution of the southern WGR

From the thermodynamic modelling, the WGC18-016 garnet records the prograde conditions during slab subduction, with initial isothermal burial between 9.5 and 14 kbar at 475 °C and then heating and burial to 19 kbar and 580 °C while clinopyroxene records up to 20 kbar and 630 °C and amphibole becomes unstable at ∼22 kbar and ∼650 °C. We test if this isothermal path is due to overstepping but find the overstepping model still requires garnet growth at higher pressure under isothermal conditions and is due to slab subduction rather than an artifact of overstepping (Fig. 10). Peak temperature modelling suggests temperature ≤ 700 °C is required to preserve the compositional zoning observed at the garnet core (Fig. 11).

The inability to reconcile (1) the lack of garnet growth and (2) the stability of zoisite and (3) the lack of amphibole at the expected peak conditions (22 kbar and 650 °C) suggests that either (1) the stability of amphibole is over-estimated and clinopyroxene is under-estimated in our thermodynamic model for our bulk rock composition that results in higher P–T conditions than recorded in the garnet and zoisite or (2) local changes in effective bulk rock composition that controls the observed zoning in garnet and stability of zoisite compared to those predicted by whole-rock phase equilibrium modelling.

The garnet growth model has lower Fe and higher Mg fractions at the rim than observed when modelling up to 22 kbar and 650 °C and suggests an extra ∼200 μm rim growth above 19 kbar and 580 °C, which is the last P–T point recorded by the garnet rims. However, it is possible that the local matrix was being depleted in garnet-forming elements, so this extra garnet was unable to grow compared to what whole-rock equilibrium predicts. This is consistent with transport-limited growth Konrad-Schmolke et al. (2005) or dissolution-

limited growth Spear and Wolfe (2018). Both mechanisms predict that the effective bulk composition at the garnet scale differs from the whole-rock. Under transport-limited growth, the surrounding matrix was depleted in garnet-forming elements faster than intergranular transport could replenish them; under dissolution-limited growth, the sluggish kinetics of reactant mineral dissolution prevented garnet from accessing the full element budget of the whole-rock. The sharp compositional boundaries and lack of diffusional modification at the garnet rims (Fig. 7 and 5b) further support the cessation of garnet growth close to the peak zoisite stability rather than the extra $\sim$200 μm garnet growth up to amphibole-out conditions and subsequent dissolution of the rim.

At the garnet rim conditions ($\sim$19 kbar, 580°C), thermodynamic modelling predicts both zoisite and amphibole should be stable under reduced conditions. However, as the P–T increases to 22 kbar and 650 °C both amphibole and zoisite are expected to become unstable. We find that decreasing H_2O in the bulk oxide composition alone cannot explain the preservation of zoisite in our sample, which reduces the stability of both amphibole and zoisite. The amphibole–zoisite paradox may reflect differences in reaction kinetics, local effective bulk composition, or the under- or over-estimations in the thermodynamic modelling. We find that the stability of zoisite suggests more reducing conditions during prograde metamorphism as it is not present from the measured bulk rock composition, which is more oxidised. Fe^{3+} depletion has been documented using micro-XANES Borfecchia et al. (2012) and flank-method EPMA Li et al. (2018) in eclogites, where dehydration may be coupled to redox reactions that modify the oxygen budget of the rock. Modelling by Groppo and Castelli (2010) linked the breakdown of lawsonite and chlorite to the release of H_2O and O_2, producing a transition from a more oxidised to a more reduced assemblage. Studies from the Western Gneiss Region further demonstrate that prograde dehydration can produce fluid-absent conditions and inhibit complete re-equilibration (Martin and Duchêne, 2015; Young and Kylander-Clark, 2015; Peterman et al., 2009). These conditions may help preserve disequilibrium assemblages and limit the extent to which the prograde mineral record is

overprinted as transport of elements through free fluid is limited due to dehydration, resulting in dissolution-limited growth. Because the available data does not uniquely reconcile the persistence of matrix zoisite with the absence of amphibole, we use the garnet-rim isopleths and the peak zoisite stability field to define a lower-bound estimate of approximately 19 kbar and 580 °C while clinopyroxene stability and lack of amphibole provide an upper-bound estimate of approximately 22 kbar and 650 °C.

Our peak P–T range is in agreement with previously published studies from the region. Simon et al. (2023) constrained pre-eclogite facies metamorphism in the Vågsøy eclogite, located roughly 70 km north of where WGC18-016 was collected, at 510–600 °C and 11–16 kbar. Peak conditions in Vågsøy were estimated at 660–680 °C but at higher pressures of 27–28 kbar, based on garnet isopleth QuiG barometry, Si-in-phengite barometry, and Zr-in-rutile thermometry. In the Outer Sunnfjord area, which is closest to where WGC18-016 was collected, Labrousse et al. (2004) reported peak burial conditions of the B8 eclogite of 525 °C and 22.7 kbar, while in the more southerly Hyllestad region, eclogite EC1 reached peak conditions of 707 °C and 24.8 kbar, both based on thermobarometery. Additional constraints provided by Martin and Duchêne (2015) from the nearby Vårdalsneset eclogite indicate metamorphic conditions of 590–720 °C and 15–25 kbar, determined through thermodynamic modelling and Fe–Mg exchange between garnet and omphacite thermometry, all of which are consistent with our results.

The P–T suggested for the southern WGR is consistent with results from numerical models of slab break-off and the exhumation of (ultra-)high pressure rocks (Duretz et al., 2012; Duretz and Gerya, 2013), where subduction of the oceanic slab below the continental margin occurs under near-isothermal conditions, followed by a brief interval of heating and minor burial during necking that lasts ∼10 Myr. After necking and subsequent slab break-off, rapid exhumation from depths greater than 100 km to the surface occurs over a similar timescale, again under near-isothermal conditions (Duretz et al., 2012; Duretz and Gerya, 2013). Our results and inferred geodynamic evolution also align with the previous interpretations for the

region, where the observed decrease in peak pressure and temperature conditions from north to south reflects the progressive decrease of exhumation depths (Labrousse et al., 2004).

4.6 Model limitations

The multicomponent diffusion modelling conducted in this study is restricted to two-dimensions within the garnet, and does not account for element diffusion across the grain boundary or local exchange with adjacent minerals after (e.g. Fe-Mg exchange between garnet and other Ferromagnesian minerals). Two-dimensional annulus geometry also underestimates diffusion at the model core relative to full three-dimensional spherical models (Fig. 4d). However, the finite element approach through `underworld3` and `UWDiffusion` provides a framework to address these limitations, as it supports spatially variable diffusion coefficients within the model domain. We plan to extend the modelling to multimaterial domains, where adjacent mineral phases are modelled explicitly, enabling intergranular element exchange (e.g. Fe-Mg exchange used in garnet-biotite or garnet-omphacite geothermometry). We also plan to extend the garnet modelling to three-dimensional grain geometries, which will resolve the cylindrical-versus-spherical discrepancy identified in our benchmarks. In subsequent work, we intend to explore both to more accurately represent element transport in garnet and other minerals. The mesh geometry can also be varied to explore more plausible mineral shapes, which has previously been explored in garnet by Gaidies et al. (2022), Wu et al. (2025) and Dominguez et al. (2026).

Conclusions

The coupled MAGEMin–UWDiffusion workflow reproduces selected analytical and published multicomponent-diffusion benchmarks and has been used to understand the evolution of the southern Western Gneiss Region. We find that:

1. **Numerical benchmarking:** The diffusion implementation reproduces analytical bi-

nary diffusion, published ternary cross-diffusion results, uphill diffusion in garnet, and planar results from CZGM. The comparisons also demonstrate that an annulus geometry underestimates diffusion relative to a fully spherical representation.

2. **Preservation of garnet zoning:** The pronounced Mn-rich/Mg-poor core to Mn-poor/Mg-rich rim zoning in sample WGC18-016 is consistent with primary growth zoning that underwent limited modification due to diffusion to preserve the observed compositions at the garnet core.

3. **Prograde metamorphic evolution:** Garnet growth initiated during near-isothermal burial at approximately 475°C between 9.5 and 14 kbar, followed by heating and further burial. The garnet rim records conditions of around 19 kbar and 580°C, while clinopyroxene records 20 kbar and 630°C and amphibole-out occurs at ∼22 kbar and 650°C.

4. **Cessation of garnet growth:** Growth modelling to approximately 22 kbar and 650°C predicts an additional ~ 200 μm of garnet and Fe–Mg compositions inconsistent with the observed rim. The garnet data therefore suggests that garnet growth ceased near the lower-bound peak conditions (19 kbar and 580°C), potentially because of local depletion of garnet-forming elements due to transport or dissolution-limited growth or local bulk-composition effects.

5. **Peak conditions:** The thermodynamic modelling of our bulk rock combined with garnet, clinopyroxene, zoisite, amphibole and rutile constraints indicate a peak range of between 19–22 kbar and 580–650°C, rather than a uniquely resolved single peak P–T estimate that satisfies all constraints.

6. **Geological interpretation:** The inferred path is consistent with near-isothermal subduction of the southern Baltica margin, followed by heating and burial and relatively rapid exhumation. This evolution is compatible with regional slab-breakoff models.

Author Contributions

BSK: Conceptualization, Methodology, Software, Validation, Formal analysis, Investigation, Writing - Original Draft, Writing - Review & Editing, Visualization, Resources. **CC**: Conceptualization, Formal analysis, Investigation, Writing - Review & Editing, Visualization, Supervision, Project administration, Funding acquisition, Resources. **ICWF**: Investigation, Writing - Review & Editing, Visualization, Supervision.

Competing Interests

All authors declare that they have no competing interests.

Code Availability

underworld3 is available from Moresi et al. (2026) (doi:10.5281/zenodo.16810746), UWDiffusion is available from Knight (2026b) (doi: 10.5281/zenodo.17936510) and PhaseTools is available from Knight (2026a) (doi: 10.5281/zenodo.21963054), all are licensed under LGPL v3. Figures were made with Matplotlib v3.10.1 (Hunter, 2007), available under the Matplotlib license at https://matplotlib.org/.

Acknowledgements

The authors acknowledge and pay our respects to the Whadjuk Nyungar people who are the Traditional Custodians of the land this research was conducted on. The authors acknowledge AuScope for their continued support in the development of the underworld code. This work was supported by resources provided by the Pawsey Supercomputing Research Centre's Setonix Supercomputer (https://doi.org/10.48569/18sb-8s43), with funding from the Australian Government and the Government of Western Australia. We thank Sean Makin for EPMA data collection.

Financial Support

This research has been supported by the Australian Research Council (grant no. FT220100566 and DP220103027).

References

Anczkiewicz, R., Szczepański, J., Mazur, S., Storey, C., Crowley, Q., Villa, I. M., Thirlwall, M. F., and Jeffries, T. E. (2007). Lu–Hf geochronology and trace element distribution

in garnet: Implications for uplift and exhumation of ultra-high pressure granulites in the Sudetes, SW Poland. *Lithos*, 95(3):363–380.

Anderson, D. E. and Buckley, G. R. (1973). Zoning in garnets—diffusion models. *Contributions to Mineralogy and Petrology*, 40(2):87–104.

Baxter, E., Caddick, M., and Dragovic, B. (2017). Garnet: A rock-forming mineral petrochronometer. *Reviews in Mineralogy and Geochemistry*, 83(1):469–533.

Borfecchia, E., Mino, L., Gianolio, D., Groppo, C., Malaspina, N., Martinez-Criado, G., Sans, J. A., Poli, S., Castelli, D., and Lamberti, C. (2012). Iron oxidation state in garnet from a subduction setting: a micro-XANES and electron microprobe ("flank method") comparative study. *Journal of Analytical Atomic Spectrometry*, 27(10):1725–1733.

Borinski, S. A., Hoppe, U., Chakraborty, S., Ganguly, J., and Bhowmik, S. K. (2012). Multicomponent diffusion in garnets i: general theoretical considerations and experimental data for fe–mg systems. *Contributions to Mineralogy and Petrology*, 164:571–586.

Boudin, L., Grec, B., and Salvarani, F. (2012). A mathematical and numerical analysis of the maxwell-stefan diffusion equations. *Discrete and Continuous Dynamical Systems-Series B*, 17(5):1427–1440.

Caddick, M. J., Konopásek, J., and Thompson, A. B. (2010). Preservation of garnet growth zoning and the duration of prograde metamorphism. *Journal of Petrology*, 51(11):2327–2347.

Castro, A. E. and Spear, F. S. (2017). Reaction overstepping and re-evaluation of peak p–t conditions of the blueschist unit sifnos, greece: implications for the cyclades subduction zone. *International Geology Review*, 59(5-6):548–562.

Chai, Z., Guo, X., Wang, L., and Shi, B. (2019). Maxwell-stefan-theory-based lattice boltzmann model for diffusion in multicomponent mixtures. *Physical Review E*, 99(2):023312.

738 Chakraborty, S. and Ganguly, J. (1991). Compositional zoning and cation diffusion in gar-
739 nets. In *Diffusion, atomic ordering, and mass transport: Selected topics in geochemistry*,
740 pages 120–175. Springer.

741 Chakraborty, S. and Ganguly, J. (1992). Cation diffusion in aluminosilicate garnets: exper-
742 imental determination in spessartine-almandine diffusion couples, evaluation of effective
743 binary diffusion coefficients, and applications. *Contributions to Mineralogy and petrology*,
744 111(1):74–86.

745 Connolly, J. (1990). Multivariable phase diagrams; an algorithm based on generalized ther-
746 modynamics. *American Journal of Science*, 290(6):666–718.

747 Crank, J. (1979). *The mathematics of diffusion*. Oxford university press.

748 Cuthbert, S., Carswell, D. A., Krogh-Ravna, E., and Wain, A. (2000). Eclogites and eclogites
749 in the western gneiss region, norwegian caledonides. *Lithos*, 52:165–195.

750 de Capitani, C. and Brown, T. H. (1987). The computation of chemical equilibrium
751 in complex systems containing non-ideal solutions. *Geochimica et Cosmochimica Acta*,
752 51(10):2639–2652.

753 Dominguez, H., Mäder, N., and Lanari, P. (2026). Simulating major element diffusion in
754 garnet using realistic 3D geometries. *Computers & Geosciences*, 206:106023.

755 Duncan, J. B. and Toor, H. (1962). An experimental study of three component gas diffusion.
756 *AIChE Journal*, 8(1):38–41.

757 Duretz, T. and Gerya, T. (2013). Slab detachment during continental collision: Influence of
758 crustal rheology and interaction with lithospheric delamination. *Tectonophysics*, 602:124–
759 140.

760 Duretz, T., Gerya, T., Kaus, B., and Andersen, T. (2012). Thermomechanical modeling of
761 slab eduction. *Journal of Geophysical Research: Solid Earth*, 117(B8).

762 Elphick, S. C., Ganguly, J., and Loomis, T. P. (1985). Experimental determination of cation
763 diffusivities in aluminosilicate garnets: I. experimental methods and interdiffusion data.
764 *Contributions to Mineralogy and Petrology*, 90(1):36–44.

765 Engvik, A. K., Austrheim, H., and Andersen, T. B. (2000). Structural, mineralogical and
766 petrophysical effects on deep crustal rocks of fluid-limited polymetamorphism, western
767 gneiss region, norway. *Journal of the Geological Society*, 157(1):121–134.

768 Evans, T. P. (2004). A method for calculating effective bulk composition modification due to
769 crystal fractionation in garnet-bearing schist: implications for isopleth thermobarometry.
770 *Journal of Metamorphic Geology*, 22(6):547–557.

771 Faryad, S. W. and Ježek, J. (2019). Compositional zoning in garnet and its modification
772 by diffusion during pressure and temperature changes in metamorphic rocks; an approach
773 and software. *Lithos*, 332:287–295.

774 Faryad, S. W., Ježek, J., and Connolly, J. A. (2022). Advantages and limitations of combined
775 diffusion-phase equilibrium modelling for pressure–temperature–time history of metamor-
776 phic rocks. *Journal of Petrology*, 63(12):egac118.

777 Fernando, G., Hauzenberger, C., Baumgartner, L., and Hofmeister, W. (2003). Modeling
778 of retrograde diffusion zoning in garnet: evidence for slow cooling of granulites from the
779 highland complex of sri lanka. *Mineralogy and Petrology*, 78(1):53–71.

780 Florence, F. P. and Spear, F. S. (1991). Effects of diffusional modification of garnet growth
781 zoning on pt path calculations. *Contributions to Mineralogy and Petrology*, 107(4):487–
782 500.

783 Gaidies, F., De Capitani, C., and Abart, R. (2008). Theria_g: a software program to numeri-
784 cally model prograde garnet growth. *Contributions to Mineralogy and Petrology*, 155:657–
785 671.

786 Gaidies, F., Heldwein, O. K. A., Yogi, M. T. A. G., Cutts, J. A., Smit, M. A., and Rice,
787 A. H. N. (2022). Testing the equilibrium model: An example from the Caledonian Kalak
788 Nappe Complex (Finnmark, Arctic Norway). *Journal of Metamorphic Geology*, 40(5):859–
789 886. _eprint: https://onlinelibrary.wiley.com/doi/pdf/10.1111/jmg.12648.

790 Gaidies, F., Morneau, Y. E., Petts, D. C., Jackson, S. E., Zagorevski, A., and
791 Ryan, J. J. (2021). Major and trace element mapping of garnet: Unravel-
792 ling the conditions, timing and rates of metamorphism of the Snowcap assem-
793 blage, west-central Yukon. *Journal of Metamorphic Geology*, 39(2):133–164. _eprint:
794 https://onlinelibrary.wiley.com/doi/pdf/10.1111/jmg.12562.

795 Ganguly, J. and Tirone, M. (1999). Diffusion closure temperature and age of a mineral
796 with arbitrary extent of diffusion: theoretical formulation and applications. *Earth and*
797 *Planetary Science Letters*, 170(1):131–140.

798 Geiser, J. (2015). Iterative solvers for the maxwell–stefan diffusion equations: Methods and
799 applications in plasma and particle transport. *Cogent Mathematics*, 2(1):1092913.

800 George, F. R. and Gaidies, F. (2017). Characterisation of a garnet population from the
801 Sikkim Himalaya: insights into the rates and mechanisms of porphyroblast crystallisation.
802 *Contributions to Mineralogy and Petrology*, 172(7):57.

803 Geuzaine, C. and Remacle, J.-F. (2009). Gmsh: A 3-d finite element mesh generator with
804 built-in pre-and post-processing facilities. *International Journal for Numerical Methods*
805 *in Engineering*, 79(11):1309–1331.

806 Green, E., White, R., Diener, J., Powell, R., Holland, T., and Palin, R. (2016). Activity–
807 composition relations for the calculation of partial melting equilibria in metabasic rocks.
808 *Journal of metamorphic Geology*, 34(9):845–869.

809 Groppo, C. and Castelli, D. (2010). Prograde P–T Evolution of a Lawsonite Eclogite from

the Monviso Meta-ophiolite (Western Alps): Dehydration and Redox Reactions during Subduction of Oceanic FeTi-oxide Gabbro. *Journal of Petrology*, 51(12):2489–2514.

Hacker, B., Andersen, T., Root, D., Mehl, L., Mattinson, J., and Wooden, J. (2003). Exhumation of high-pressure rocks beneath the solund basin, western gneiss region of norway. *Journal of Metamorphic Geology*, 21(6):613–629.

Hacker, B. R., Andersen, T. B., Johnston, S., Kylander-Clark, A. R. C., Peterman, E. M., Walsh, E. O., and Young, D. (2010). High-temperature deformation during continental-margin subduction & exhumation: The ultrahigh-pressure western gneiss region of norway. 480(1):149–171.

Hacker, B. R., Kylander-Clark, A. R., Holder, R., Andersen, T. B., Peterman, E. M., Walsh, E. O., and Munnikhuis, J. K. (2015). Monazite response to ultrahigh-pressure subduction from u–pb dating by laser ablation split stream. *Chemical Geology*, 409:28–41.

Holder, R. M., Hacker, B. R., Kylander-Clark, A. R., and Cottle, J. M. (2015). Monazite trace-element and isotopic signatures of (ultra) high-pressure metamorphism: Examples from the western gneiss region, norway. *Chemical Geology*, 409:99–111.

Holland, T. and Powell, R. (2011). An improved and extended internally consistent thermodynamic dataset for phases of petrological interest, involving a new equation of state for solids. *Journal of metamorphic Geology*, 29(3):333–383.

Hollister, L. S. (1966). Garnet zoning: an interpretation based on the rayleigh fractionation model. *Science*, 154(3757):1647–1651.

Hunter, J. D. (2007). Matplotlib: A 2d graphics environment. *Computing in Science & Engineering*, 9(3):90–95.

Knight, B. (2026a). bknight1/phasetools: v0.1.0 — FeOt redox basis, instance-aware Fe split, MagmaOcean + fractionation fixes.

834 Knight, B. (2026b). bknight1/UWDiffusion: Multicomponent diffusion.

835 Knight, B. S. and Clark, C. (2026). Modelling diffusion, decay and ingrowth of u–pb isotopes
836 in zircon. *Geoscientific Model Development*, 19(14):6571–6586.

837 Kohn, M. J. (2020). A refined zirconium-in-rutile thermometer. *American Mineralogist*,
838 105(6):963–971.

839 Konrad-Schmolke, M., Handy, M. R., Babist, J., and O'Brien, P. J. (2005). Thermody-
840 namic modelling of diffusion-controlled garnet growth. *Contributions to Mineralogy and*
841 *Petrology*, 149(2):181–195.

842 Kylander-Clark, A. R., Hacker, B. R., Johnson, C. M., Beard, B. L., and Mahlen, N. J.
843 (2009). Slow subduction of a thick ultrahigh-pressure terrane. *Tectonics*, 28(2).

844 Labrousse, L., Jolivet, L., Andersen, T., Agard, P., Hébert, R., Maluski, H., and Schärer,
845 U. (2004). Pressure-temperature-time deformation history of the exhumation of ultra-
846 high pressure rocks in the western gneiss region, norway. In *Gneiss Domes in Orogeny*.
847 Geological Society of America.

848 Lanari, P. and Engi, M. (2017). Local Bulk Composition Effects on Metamorphic Mineral
849 Assemblages. *Reviews in Mineralogy and Geochemistry*, 83(1):55–102.

850 Lanari, P., Giuntoli, F., Loury, C., Burn, M., and Engi, M. (2017). An inverse modeling
851 approach to obtain P–T conditions of metamorphic stages involving garnet growth and
852 resorption. *European Journal of Mineralogy*, 29(2):181–199.

853 Lasaga, A. C. (1979). Multicomponent exchange and diffusion in silicates. *Geochimica et*
854 *Cosmochimica Acta*, 43(4):455–469.

855 Li, X., Song, S., Zhang, L., and Höfer, E. H. (2018). Application of microprobe-based flank
856 method analysis of Fe 3+ in garnet of North Qilian eclogite and its geological implication.
857 *Science Bulletin*, 63(5):300–305.

Llovet, X. (2018). Electron Probe Microanalysis. In *Reference Module in Chemistry, Molecular Sciences and Chemical Engineering*, page B9780124095472143690. Elsevier.

Loomis, T. P., Ganguly, J., and Elphick, S. C. (1985). Experimental determination of cation diffusivities in aluminosilicate garnets: Ii. multicomponent simulation and tracer diffusion coefficients. *Contributions to Mineralogy and Petrology*, 90(1):45–51.

Loomis, T. P. and Nimick, F. B. (1982). Equilibrium in mn-fe-mg aluminous pelitic compositions and the equilibrium growth of garnet. *The Canadian Mineralogist*, 20(3):393–410.

Mackay-Champion, T. and Cawood, I. (2026). An inverse method for quantifying petrological parameters and uncertainty in phase equilibrium modelling. *Journal of Metamorphic Geology*, 44(1):70–84.

March, S., Hand, M., Tamblyn, R., Carvalho, B. B., and Clark, C. (2022). A diachronous record of metamorphism in metapelites of the western gneiss region, norway. *Journal of Metamorphic Geology*, 40(6):1121–1158.

Martin, C. and Duchêne, S. (2015). Residual water in hydrous minerals as a kinetic factor for omphacite destabilization into symplectite in the eclogites of vårdalsneset (wgr, norway). *Lithos*, 232:162–173.

Martin, C., Duchêne, S., Luais, B., Goncalves, P., Deloule, E., and Fournier, C. (2010). Behavior of trace elements in relation to lu–hf and sm–nd geochronometers during metamorphic dehydration–hydration in the hp domain of vårdalsneset, western gneiss region, norway. *Contributions to Mineralogy and Petrology*, 159:437–458.

Martin, C. and Duchêne, S. (2015). Residual water in hydrous minerals as a kinetic factor for omphacite destabilization into symplectite in the eclogites of Vårdalsneset (WGR, Norway). *Lithos*, 232:162–173.

Maxwell, J. C. (1867). Iv. on the dynamical theory of gases. *Philosophical transactions of the Royal Society of London*, (157):49–88.

Meurer, A., Smith, C. P., Paprocki, M., Čertík, O., Kirpichev, S. B., Rocklin, M., Kumar, A., Ivanov, S., Moore, J. K., Singh, S., Rathnayake, T., Vig, S., Granger, B. E., Muller, R. P., Bonazzi, F., Gupta, H., Vats, S., Johansson, F., Pedregosa, F., Curry, M. J., Terrel, A. R., Roučka, v., Saboo, A., Fernando, I., Kulal, S., Cimrman, R., and Scopatz, A. (2017). Sympy: symbolic computing in python. *PeerJ Computer Science*, 3:e103.

Moresi, L., Giordani, J., Knepley, M., Beucher, R., Gollapalli, T., Graciosa, J. C., Knight, B., Lu, N., Mansour, J., and Beucher, R. (2026). Underworld3: Mathematically Self-Describing Modelling in Python for Desktop, HPC and Cloud.

Moresi, L., Mansour, J., Giordani, J., Knepley, M., Knight, B., Graciosa, J. C., Gollapalli, T., Lu, N., and Beucher, R. (2025). Underworld3: Mathematically self-describing modelling in python for desktop, hpc and cloud. *Journal of Open Source Software*, 10(112):7831.

Moynihan, D. P. and Pattison, D. R. M. (2013). An automated method for the calculation of P–T paths from garnet zoning, with application to metapelitic schist from the Kootenay Arc, British Columbia, Canada. *Journal of Metamorphic Geology*, 31(5):525–548.

Nagurney, A. B., Caddick, M. J., Dragovic, B., and Busse, K. (2021). The (chemical) potential for understanding overstepped garnet nucleation and growth. *American Mineralogist*, 106(5):812–829.

Pattison, D. and Bégin, N. (1994). Zoning patterns in orthopyroxene and garnet in granulites: implications for geothermometry. *Journal of Metamorphic Geology*, 12(4):387–410.

Perchuk, A. and Philippot, P. (1997). Rapid cooling and exhumation of eclogitic rocks from the great caucasus, russia. *Journal of Metamorphic Geology*, 15(3):299–310.

Peterman, E. M., Hacker, B. R., and Baxter, E. F. (2009). Phase transformations of continental crust during subduction and exhumation: Western gneiss region, norway. 21(6):1097–1118.

Qiang, J. (2014). A unified differential evolution algorithm for global optimization.

Riel, N., Kaus, B. J., Green, E., and Berlie, N. (2022). Magemin, an efficient gibbs energy minimizer: application to igneous systems. *Geochemistry, Geophysics, Geosystems*, 23(7):e2022GC010427.

Ritchie, N. W. M. and Newbury, D. E. (2012). Uncertainty Estimates for Electron Probe X-ray Microanalysis Measurements. *Analytical Chemistry*, 84(22):9956–9962.

Root, D. B., Hacker, B. R., Gans, P. B., Ducea, M. N., Eide, E. A., and Mosenfelder, J. L. (2005). Discrete ultrahigh-pressure domains in the western gneiss region, norway: implications for formation and exhumation. *Journal of Metamorphic Geology*, 23:45–61.

Rowley, C. (2022). Pythoncall.jl: Python and julia in harmony.

Simon, M., Pitra, P., Yamato, P., and Poujol, M. (2023). Isothermal compression of an eclogite from the western gneiss region (norway). *Journal of Metamorphic Geology*, 41(1):181–203.

Smit, M. A., Scherer, E. E., and Mezger, K. (2013). Peak metamorphic temperatures from cation diffusion zoning in garnet. *Journal of Metamorphic Geology*, 31(3):339–358. _eprint: https://onlinelibrary.wiley.com/doi/pdf/10.1111/jmg.12024.

Spear, F. S. (1989). Relative thermobarometry and metamorphic pt, paths. *Geological Society, London, Special Publications*, 43(1):63–81.

Spear, F. S. and Selverstone, J. (1983). Quantitative pt paths from zoned minerals: Theory and tectonic applications. *Contributions to Mineralogy and Petrology*, 83(3):348–357.

927 Spear, F. S., Selverstone, J., Hickmott, D., Crowley, P., and Hodges, K. (1984). Pt paths
928 from garnet zoning: A new technique for deciphering tectonic processes in crystalline
929 terranes. *Geology*, 12(2):87–90.

930 Spear, F. S., Thomas, J. B., and Hallett, B. W. (2014). Overstepping the garnet isograd: a
931 comparison of quig barometry and thermodynamic modeling. *Contributions to Mineralogy*
932 *and Petrology*, 168(3):1059.

933 Spear, F. S. and Wolfe, O. M. (2018). Evaluation of the effective bulk composition (EBC)
934 during growth of garnet. *Chemical Geology*, 491:39–47.

935 Spear, F. S. and Wolfe, O. M. (2019). Implications of overstepping of garnet nucleation for
936 geothermometry, geobarometry and P–T path calculations. *Chemical Geology*, 530:119323.

937 Stefan, J. (1871). Über das gleichgewicht und die bewegung, insbesondere die diffusion von
938 gasgemengen. *Sitzber. Akad. Wiss. Wien*, 63:63–124.

939 Tinkham, D. K. and Ghent, E. D. (2005). Estimating pt conditions of garnet growth with
940 isochemical phase-diagram sections and the problem of effective bulk-composition. *The*
941 *Canadian Mineralogist*, 43(1):35–50.

942 Tracy, R. J., Robinson, P., and Thompson, A. B. (1976). Garnet composition and zoning in
943 the determination of temperature and pressure of metamorphism, central massachusetts.
944 *American mineralogist*, 61(7-8):762–775.

945 Vielzeuf, D. and Saúl, A. (2011). Uphill diffusion, zero-flux planes and transient chemical
946 solitary waves in garnet. *Contributions to Mineralogy and Petrology*, 161(5):683–702.

947 Waters, D. and Lovegrove, D. (2002). Assessing the extent of disequilibrium and overstepping
948 of prograde metamorphic reactions in metapelites from the bushveld complex aureole,
949 south africa. *Journal of Metamorphic Geology*, 20(1):135–149.

Weyer, Jarick, and Mezger (1999). Quantitative temperature-time information from retrograde diffusion zoning in garnet: constraints for the p–t–t history of the central black forest, germany. *Journal of Metamorphic Geology*, 17(4):449–461.

White, R. W., Powell, R., and Johnson, T. E. (2014). The effect of Mn on mineral stability in metapelites revisited: new a–x relations for manganese-bearing minerals. *Journal of Metamorphic Geology*, 32(8):809–828. _eprint: https://onlinelibrary.wiley.com/doi/pdf/10.1111/jmg.12095.

Wu, H., Zeng, L., Ge, R., and Zhu, W. (2025). Finite Element Method for Garnet Diffusion Chronometry. *Geochemistry, Geophysics, Geosystems*, 26(4):e2025GC012182. _eprint: https://agupubs.onlinelibrary.wiley.com/doi/pdf/10.1029/2025GC012182.

Young, D. J. and Kylander-Clark, A. R. C. (2015). Does continental crust transform during eclogite facies metamorphism? *Journal of Metamorphic Geology*, 33(4):331–357. _eprint: https://onlinelibrary.wiley.com/doi/pdf/10.1111/jmg.12123.

List of Figures

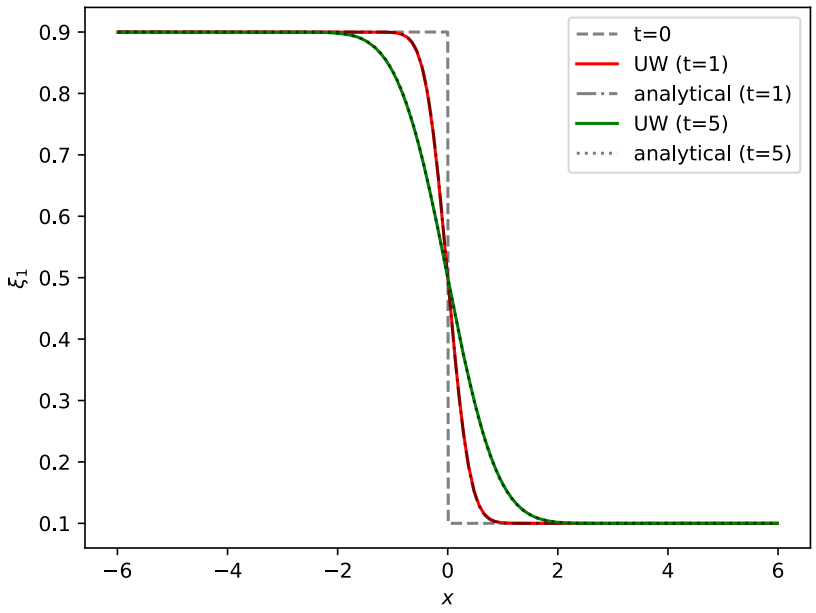

Figure 1: The profiles for concentration ξ_1 at different times comparing the analytical (Eq. 15) and numerical solution from `UWDiffusion` (UW) at y=0.

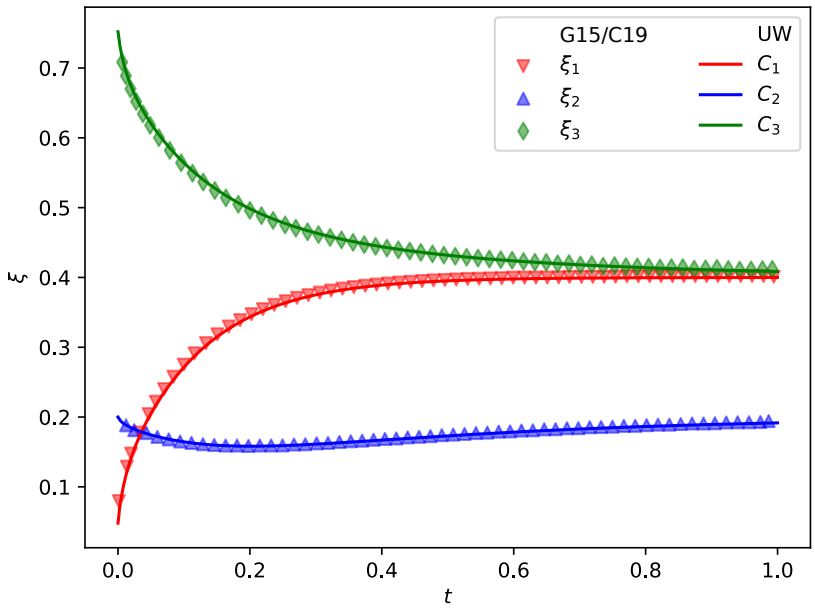

Figure 2: The profiles for concentrations ξ_1, ξ_2 and ξ_3 over time from `UWDiffusion` (UW), sampled at point x=0.72 y=0.5. Comparative numerical results are from Geiser (2015) (G15) and Chai et al. (2019) (C19).

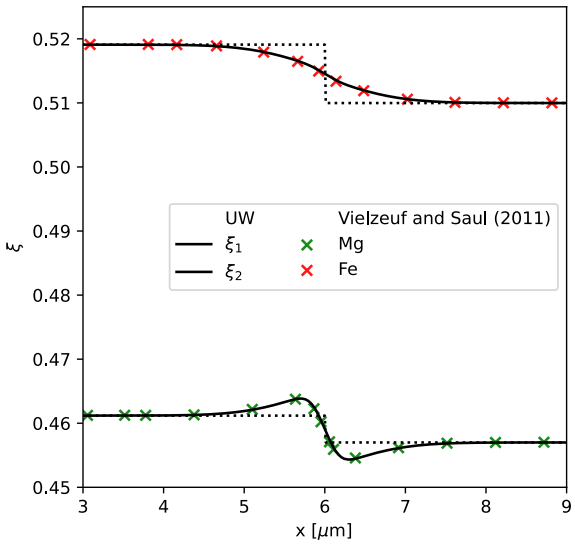

Figure 3: Initial profiles and diffused profiles for Mg and Fe (Ca = 1 - Mg - Fe) from `UWDiffusion` (UW) compared with profiles from Vielzeuf and Saúl (2011) after 6 days of diffusion, with uphill diffusion of Mg caused by the coupling.

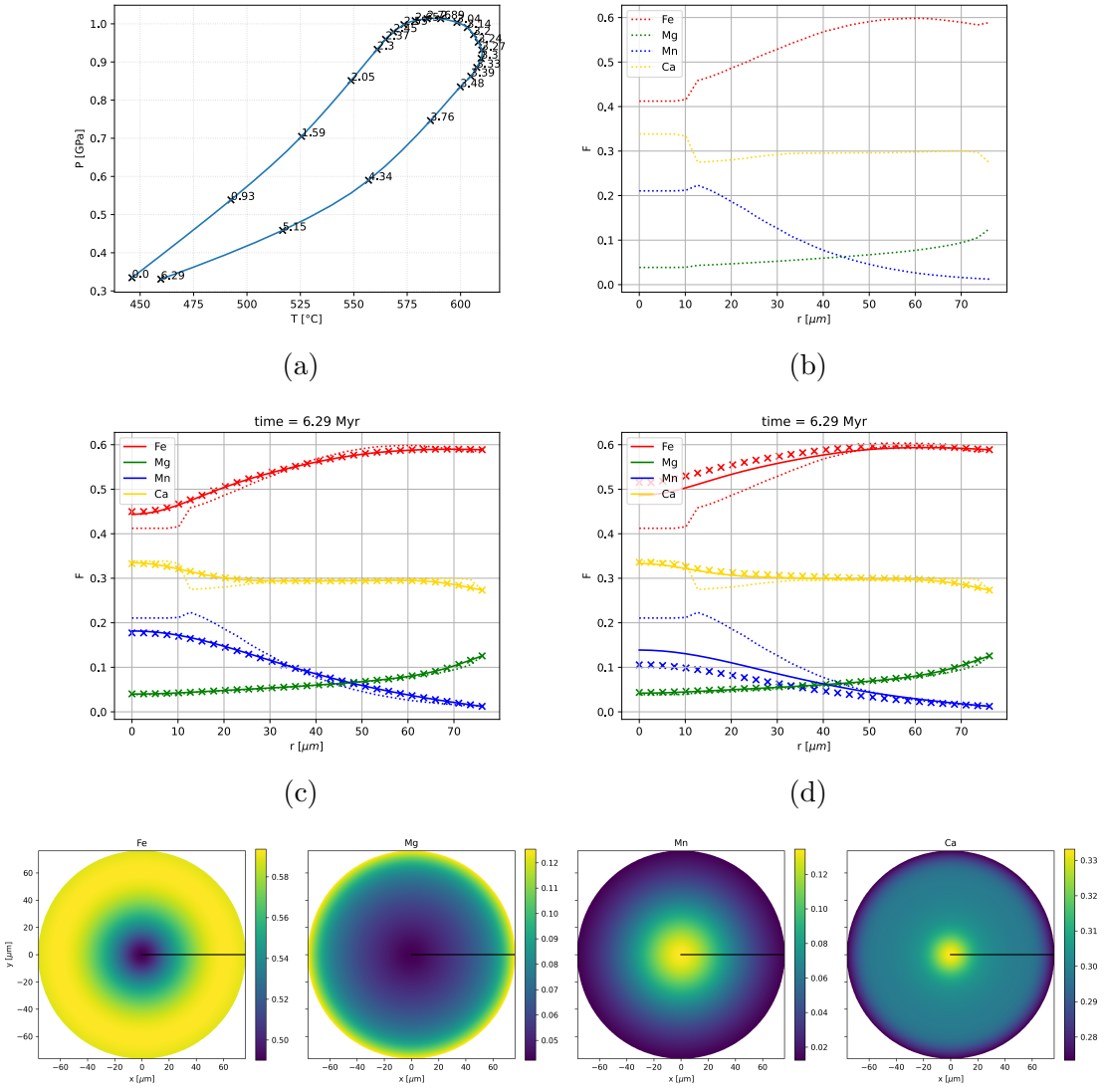

Figure 4: a) P–T–t path over which the garnet grows and diffuses from $CZGM$. b) Garnet major element end-member fractions (F) from core to rim without diffusion from $CZGM$ (dotted lines). Comparison of results between $CZGM$ (crosses) and `UWDiffusion` (solid lines) implementation of multi-component diffusion within garnets c) in a planar geometry and d) comparing spherical (CZGM) and 2D cylindrical in Cartesian (UWDiffusion). e) Model results in annulus domain for each element in garnet, black line denotes the profile in (d).

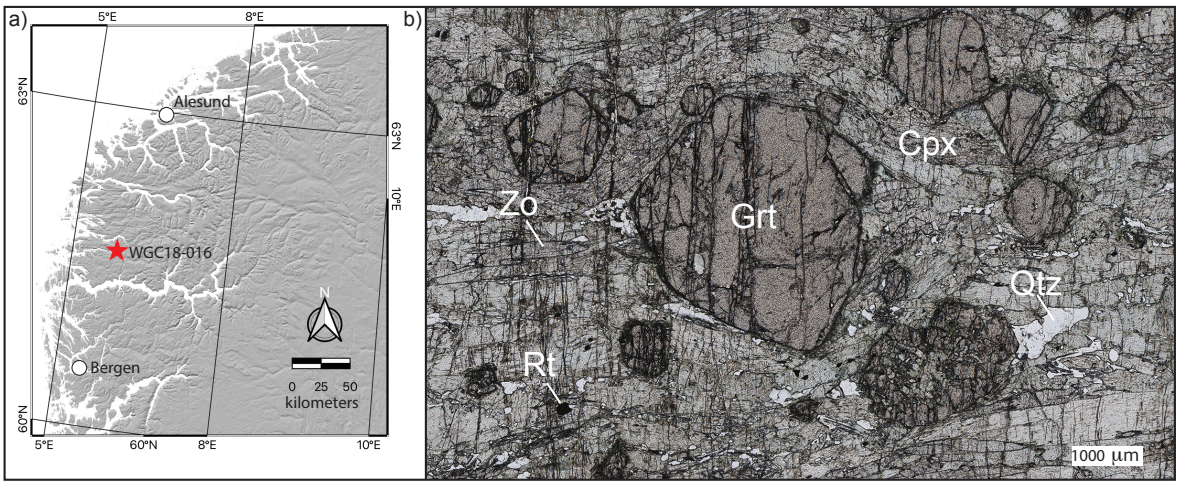

Figure 5: a) Map of the study area showing the sample location b) plane-polarised light (PPL) image for sample WGC18-016.

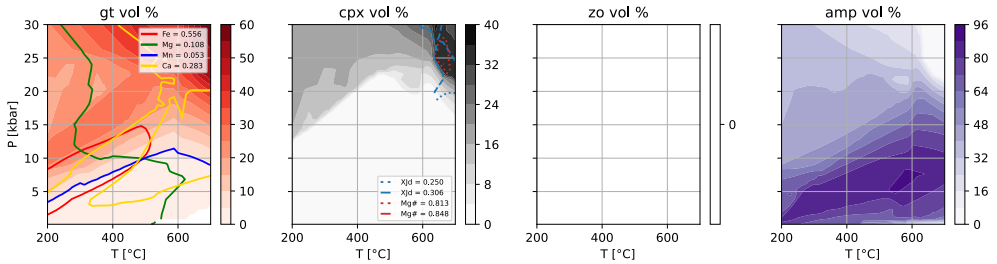

(a)

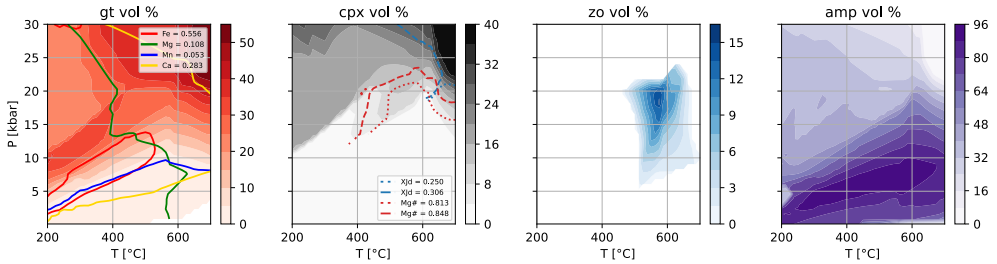

(b)

Figure 6: Comparison of phases volumes using the a) measured and b) reduced bulk rock compositions. Clinopyroxene and garnet compositions were determined from electron microprobe analyses by converting oxide wt% to mol% and computing cation fractions: jadeite fraction (X_{Jd}) as $2\mathrm{Na_2O}/(2\mathrm{Na_2O} + \mathrm{CaO})$ and Mg# as $\mathrm{MgO}/(\mathrm{MgO} + \mathrm{FeO_t})$ for clinopyroxene, and X-site end-member fractions (X_{Alm}, X_{Py}, X_{Grs}, X_{Spss}) from $\mathrm{Fe^{2+}}$, $\mathrm{Mg^{2+}}$, $\mathrm{Ca^{2+}}$, and $\mathrm{Mn^{2+}}$ for garnet.

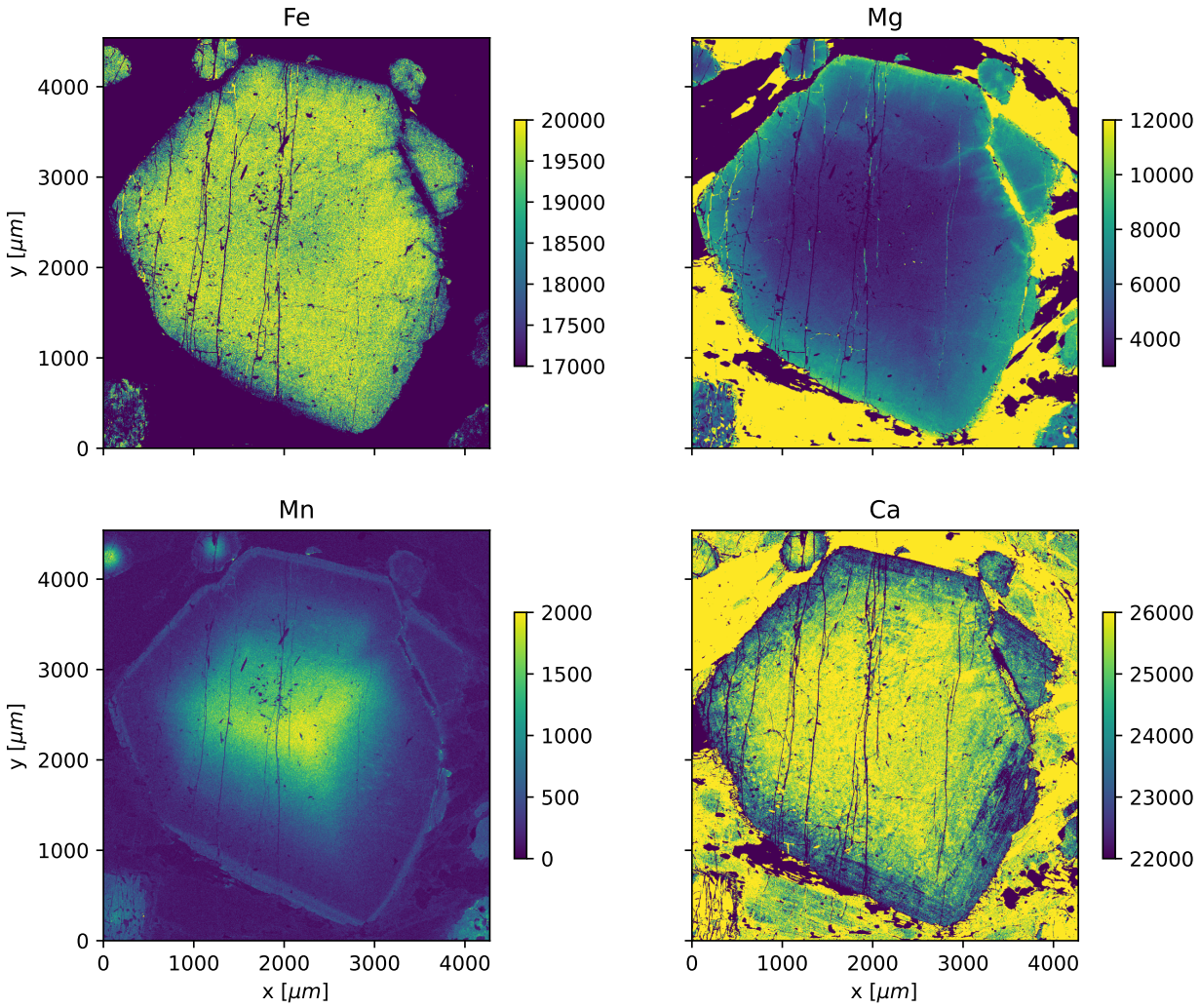

Figure 7: Intensity maps (counts per second) for each garnet element from sample WGC18-016.

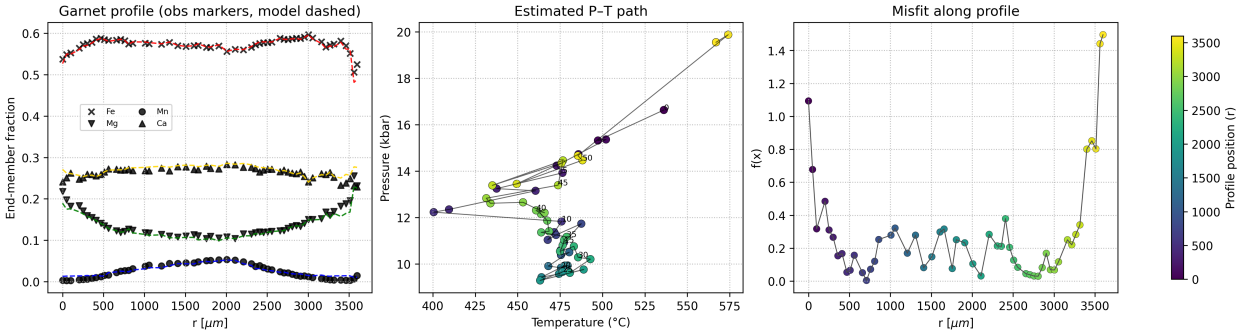

Figure 8: Results of intersecting isopleths minimisation assuming no fractionation. a) Comparison of observation EPMA data (markers) with that expected from the thermodynamic modelling (dashed line) at the predicted P–T point, as shown in b). c) Shows the value obtained from Eq. 1.

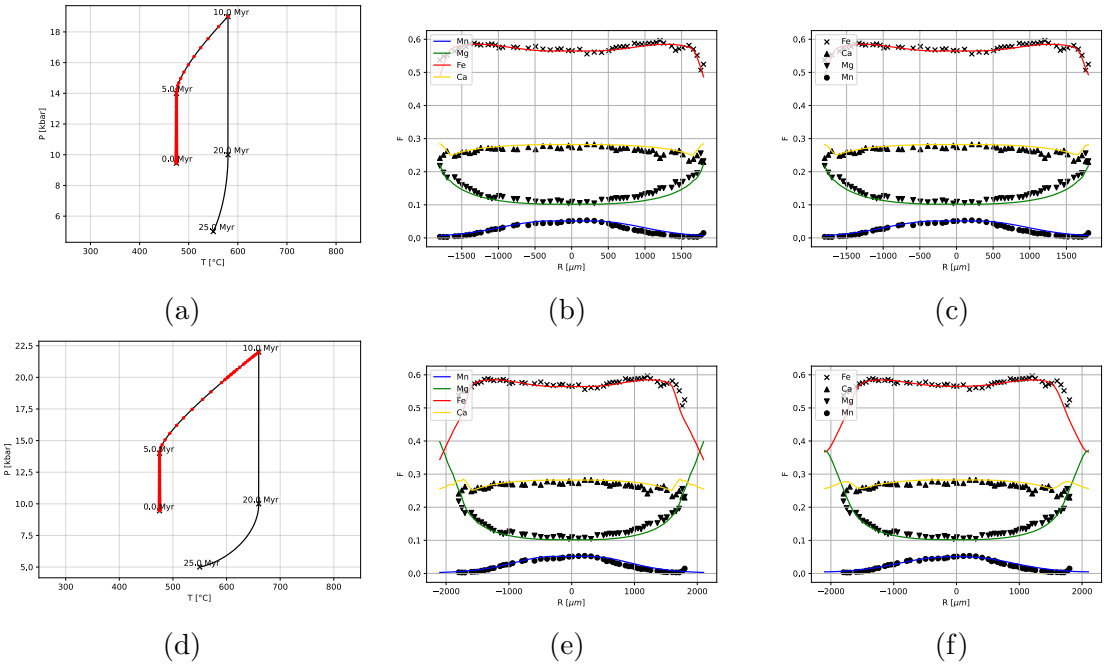

Figure 9: Comparison of growth paths up to varying peak conditions. Top row is constrained by the zoisite peak stability and garnet rim end-members. Bottom row is constrained by the amphibole-out. A) P-T-t path with red dots showing growth locations. B) End-member zoning due to growth only. C) End-member zoning after growth and diffusion. D) P-T-t path with red dots showing growth locations. E) End-member zoning due to growth only. F) End-member zoning after growth and diffusion. with minor modifications at the rim. Both diffusion models show minor modification due to the low temperature and large garnet size. The main difference is in garnet composition at the rim, with the higher P–T garnet (bottom row) displaying much higher Mg and lower Fe at the rim compared to the lower P–T garnet (top row).

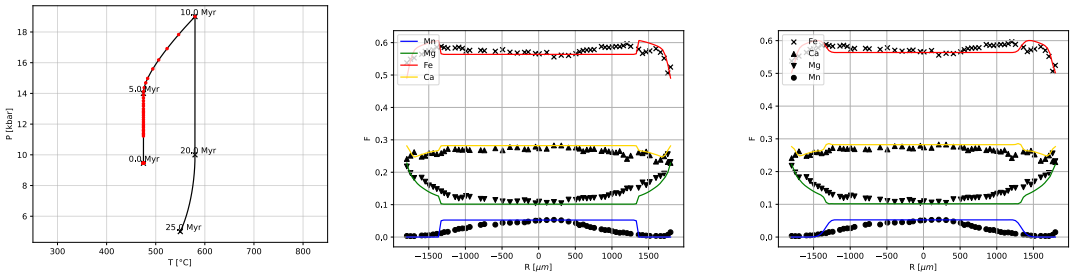

(a) (b) (c)

Figure 10: Garnet end-member profiles due to overstepped growth. a) P–T–t plot of the overstepped model showing the garnet growth locations, with a jump between the initial growth and subsequent growth due to overstepping. b) garnet end-members after growth only (no diffusion) due to overstepping. c) Final garnet end-members after growth and diffusion for the overstepped model.

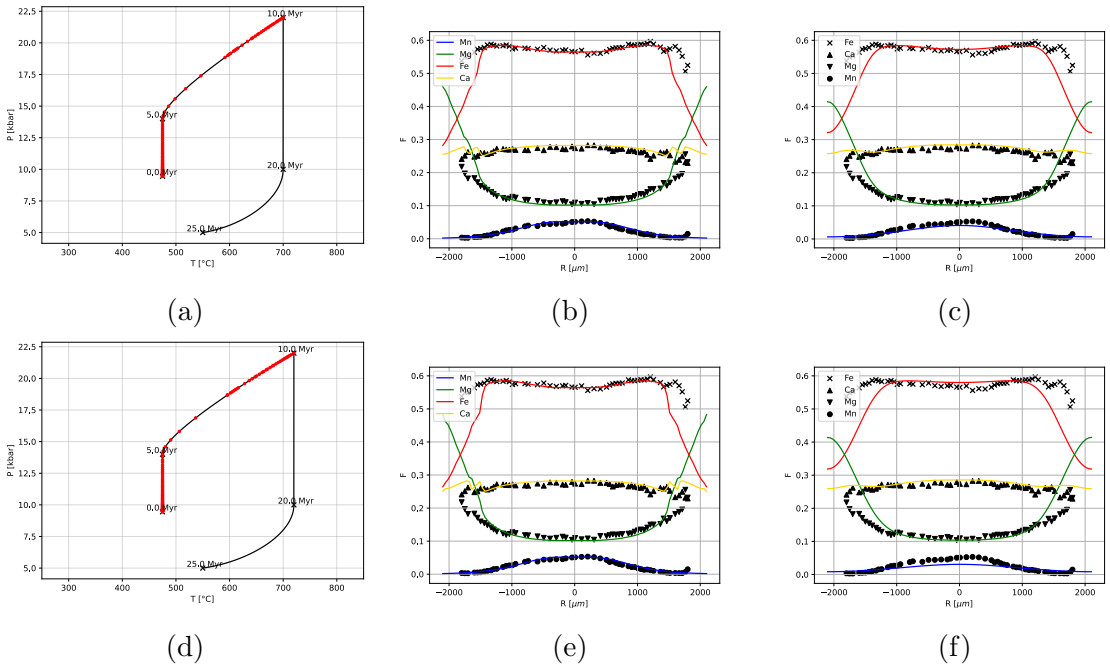

Figure 11: Sensitivity of the preservation of garnet compositional zoning to peak temperature. a) The P–T–t path and garnet growth locations, b) the growth profile only and c) compositional zoning after growth and diffusion, with the compositional zoning from core to rim well preserved. d) The P–T–t path and garnet growth locations, e) the growth profile only and f) compositional zoning after growth and diffusion, with the compositional zoning showing modification, primarily at the garnet core.

Supplementary material for: Reconstructing the P–T–t evolution recorded in garnet through growth and multicomponent diffusion modelling

Ben S. Knight* Chris Clark* Ian C.W. Fitzsimons*

August 18, 2026

S1 Whole rock geochemistry

The sample for the whole rock geochemistry was cut from the sample adjacent to thin section blocks to provide the best representation of thin section composition. The bulk major element compositions of the samples were measured by x-ray fluorescence (XRF) at Franklin and Marshall College, Pennsylvania using a PANalytical 2404 X-ray fluorescence vacuum spectrometer by fusing 0.4000g of sample with 3.6000g of lithium tetraborate. Major oxides; SiO2, Al2O3, CaO, K2O, P2O5, TiO2, total iron (Fe2O3T), MnO, Na2O and MgO along with selected trace elements were measured by XRF. FeO/Fe2O3 was measured by titration, while H2O was measured through loss on ignition (LOI) by heating the sample to 900–950 °C for 60 minutes.

*School of Earth and Planetary Sciences, Curtin University, Australia. Corresponding author: ben.knight@curtin.edu.au

Table 1: Measured major oxide geochemical composition (wt%)

Oxide	SiO_2	TiO_2	Al_2O_3	$Fe_2O_3^T$	MnO	MgO	CaO	Na_2O	K_2O	P_2O_5	Total	LOI	FeO	Fe_2O_3
wt%	46.99	0.04	15.82	11.62	0.14	11.57	12.06	1.47	0.09	0.04	99.83	2.16	8.27	2.43

S2 EPMA analysis

Electron microprobe analysis was conducted to determine quantitative mineral compositions and obtain elemental maps for Fe, Al, Ca, Mg and Mn of garnet at Adelaide Microscopy, University of Adelaide using a Cameca SXFive Electron Microprobe equipped with 5 tuneable wavelength-dispersive spectrometers running Probe for EPMA software. A 15 KeV acceleration voltage, 20 nA beam current with 2 μm defocused beam size was used for each mineral composition analysis, at an average of 90 seconds per analysis. The following suite of elements was acquired: Cl, Ca, K, Ba, F, Ti, P, Na, Si, Mg, Al, Fe, Mn, Cr, Zn, and Ni, oxygen was calculated by stoichiometry, assuming that all Fe was Fe2+. Calibration was to a wide range of synthetic and natural standards within Probe for EPMA software, with the software used to convert CPS to wt%. Elemental maps were acquired with a 15 KeV acceleration voltage, 200 nA beam current with a defocused beam size varying (2–5 μm) between samples. The data is available in the supplementary material.

S3 Additional figures

References

Kohn, M. J. (2020). A refined zirconium-in-rutile thermometer. *American Mineralogist*, 105(6):963–971.

List of Figures

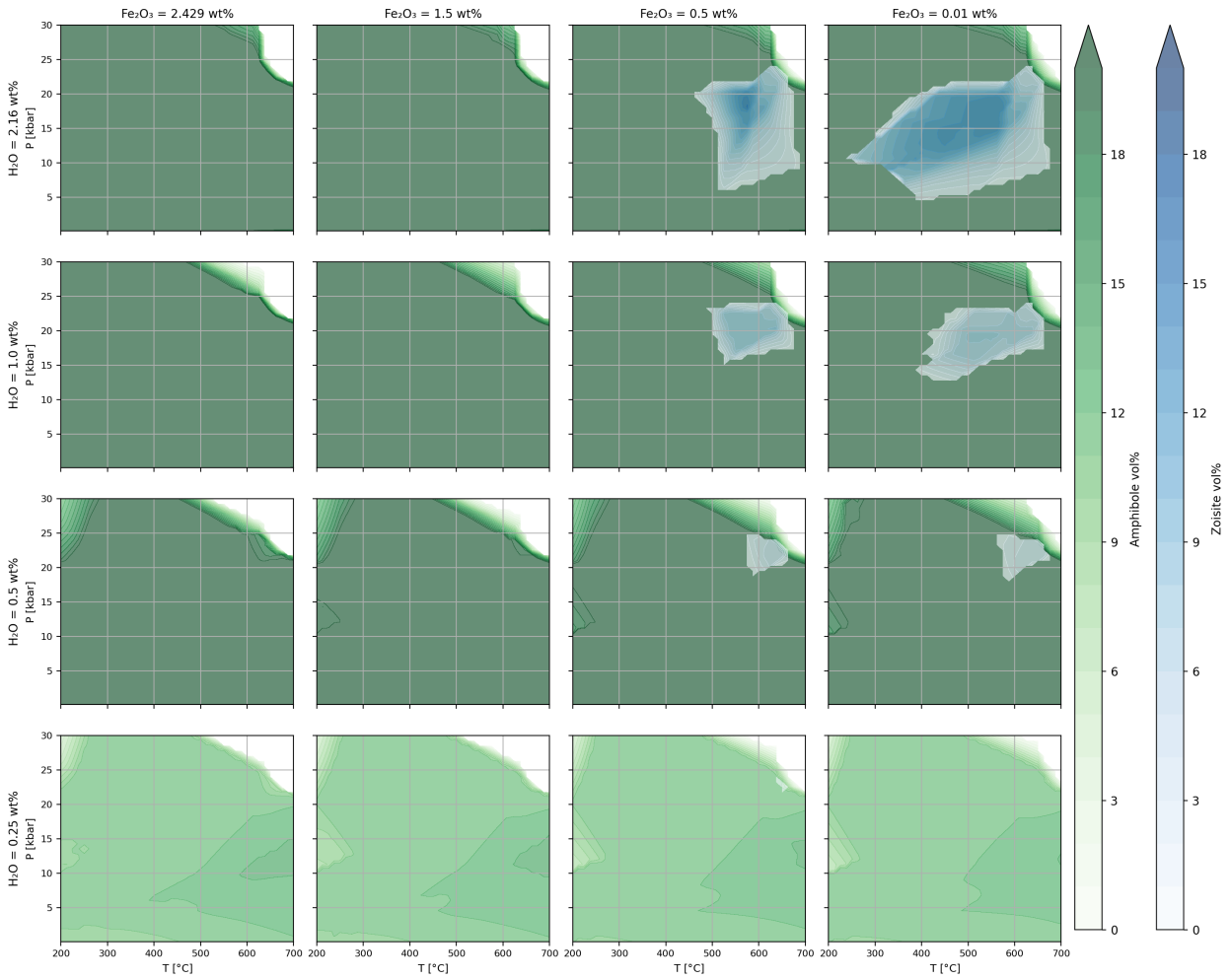

Figure S1: A comparison of amphibole (amp) and zoisite (zo) stability in P–T space for a range of redox and hydration states using the metapelite extended database and 6.36 dataset.

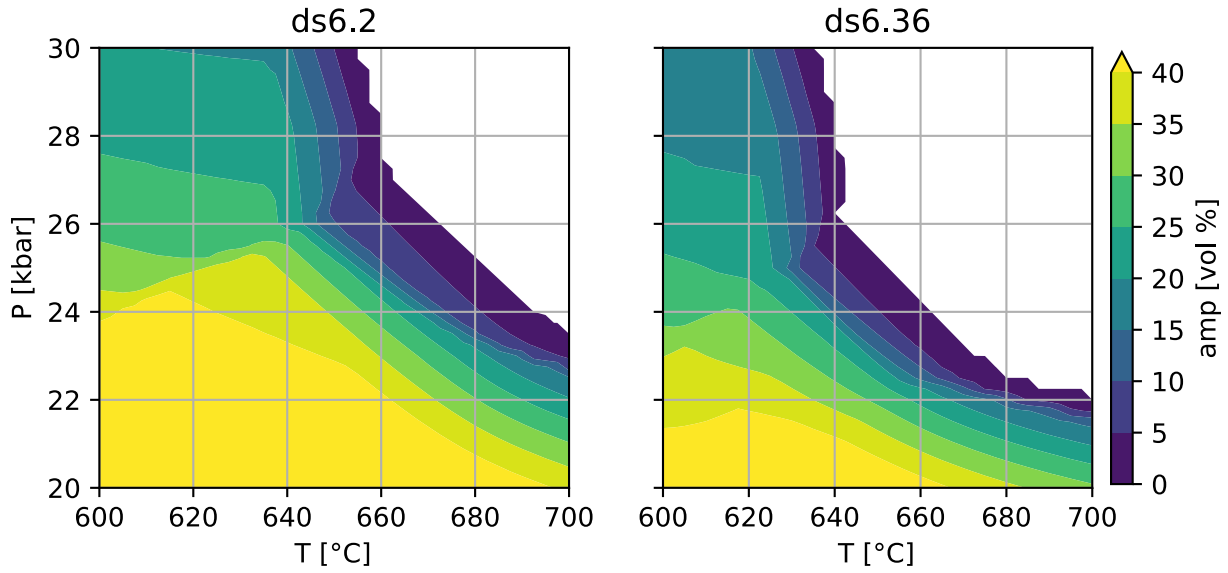

Figure S2: A comparison of estimated amphibole volume for the measured bulk rock composition from table 2 for different datasets (6.2 and 6.36) using the metapelite extended database. The models highlight how amphibole-out occurs at slightly lower P–T conditions in dataset 6.36 compared to 6.2, suggesting that the amphibole solution model may not be well calibrated at close to eclogite facies conditions.

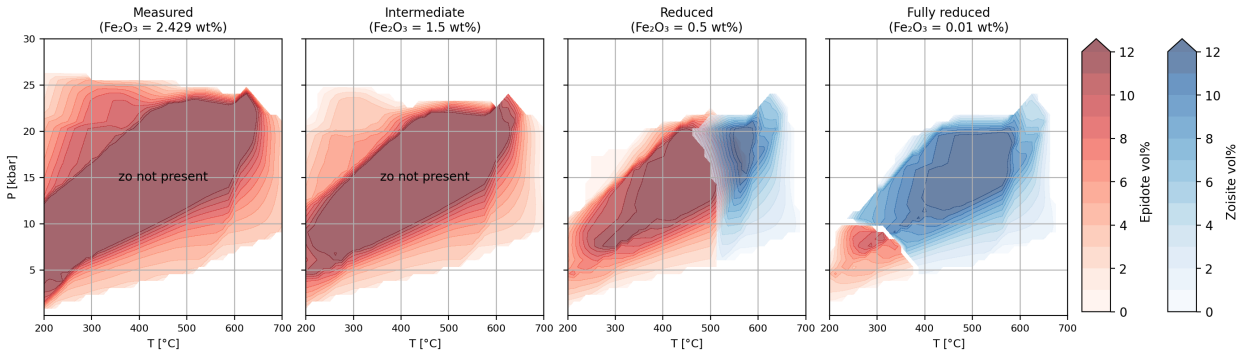

Figure S3: A comparison of epidote (ep) and zoisite (zo) stability in P–T space for a range of redox states using the metapelite extended database and 6.36 dataset. As the Fe_2O_3 decreases for a fixed FeOt, zoisite becomes more stable while epidote becomes less stable at a fixed H_2O content, with values modified from the measured bulk rock in wt%.

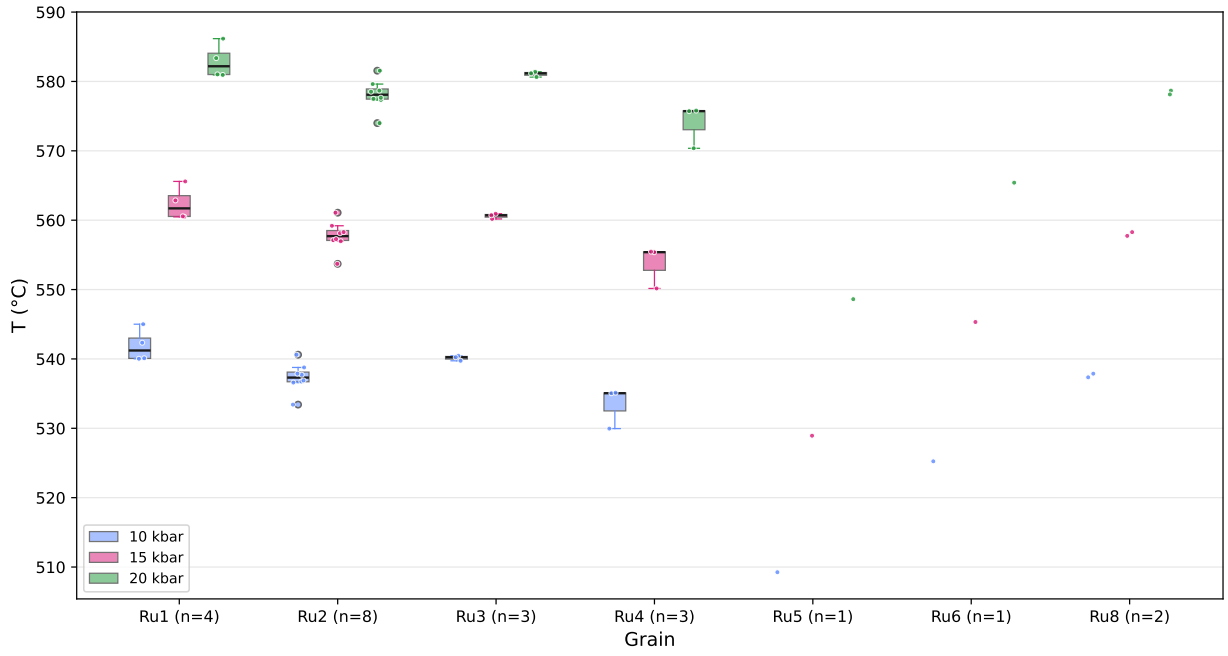

Figure S4: Zirconium in rutile temperature estimates using the Kohn (2020) thermometer at 10, 15 and 20 kbar.

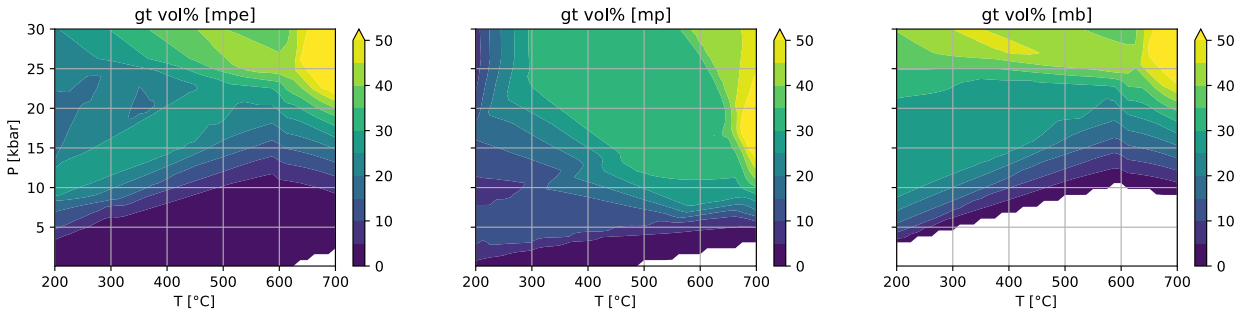

Figure S5: A comparison of estimated garnet volume for the measured bulk rock composition from table 2 for different thermodynamic databases (metapelite extended - mpe and metabasite - mb) using the 6.36 dataset. The models highlight how garnet is stabilised at lower P–T conditions due to the combination of the metapelite (mp) and metabasite (mp) dataset. The metabasite being more representative of the sample, that has an elevated garnet-in isopleth, while the inclusion of MnO in the metapelite extended (mpe) dataset results in garnet being stabilised (at low volumes) at lower P–T conditions, similar to the metapelite (mp) database.

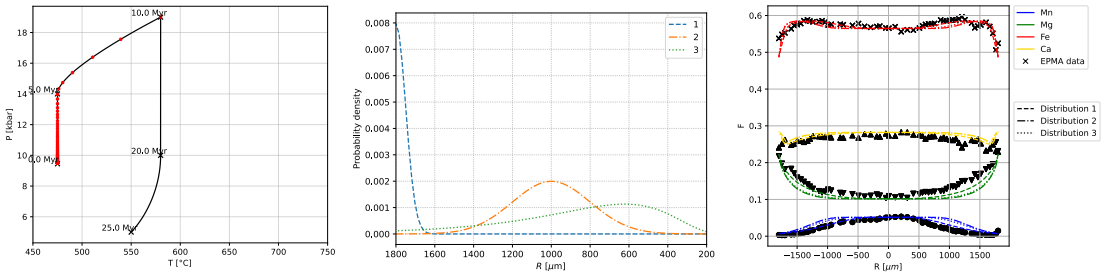

(a) (b) (c)

Figure S6: a) PT path used to test different crystal size distributions. b) Probability density plots for the three tested crystal size distributions. c) Resulting garnet compositional zoning based on the crystal size distribution.

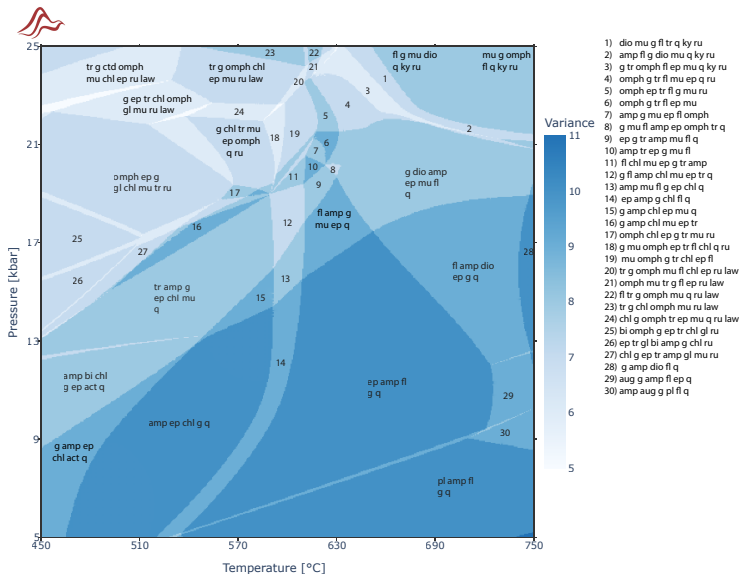

(a)

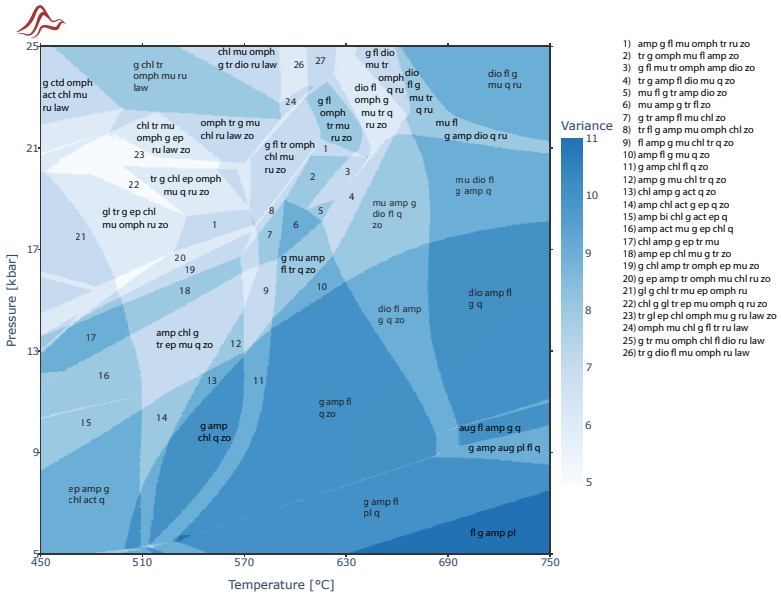

(b)

Figure S7: Pseudosections for a) the measured and b) reduced bulk rock compositions from table 2 in the main text using the metapelite extended database and 6.36 dataset. Reduced conditions extend diopside stability to higher pressures.